

# All-Optical Method of Nanoscale Magnetometry for Ensembles of Nitrogen-Vacancy Defects in Diamond

By

=====

Submitted to the  
DEPARTMENT OF NUCLEAR SCIENCE AND ENGINEERING

In Partial Fulfillment for the Degree of  
BACHELOR OF SCIENCE IN NUCLEAR SCIENCE AND ENGINEERING

At the  
MASSACHUSETTS INSTITUTE OF TECHNOLOGY

June 2015

©2015 =====. All Rights Reserved.

The author hereby grants to MIT permission to reproduce and  
to distribute publicly paper and electronic copies of this thesis  
document in whole or in part.

Signature of Author:

\_\_\_\_\_

=====

Department of Nuclear Science & Engineering

May 8, 2015

Certified by:

\_\_\_\_\_

=====

-----

Thesis Supervisor

Approved by:

\_\_\_\_\_

Dennis Whyte

Professor of Nuclear Science & Engineering  
Chair, NSE Committee for Undergraduate Students

# All-Optical Method of Nanoscale Magnetometry for Ensembles of Nitrogen-Vacancy Defects in Diamond

=====

Submitted to the Department of Nuclear Science and Engineering in partial fulfillment of the requirements for the degree of Bachelor of Science in Nuclear Science and Engineering

## ABSTRACT

The Nitrogen-Vacancy (NV) defect in diamond has shown considerable promise in the field of small scale magnetometry due to its high localization and its retention of favorable optical properties in ambient conditions. Present methods of magnetometry with the NV center demonstrate high sensitivity to fields aligned with the defect axis; however, with most present methods transverse fields are not directly measurable. The all-optical method of NV magnetometry provides a means to detect transverse fields by monitoring changes in the overall fluorescence profile. In this work the all-optical method is extended to ensembles of non-interacting NV centers. By establishing an external bias field aligned with the  $(1,1,1)$  axis it is found that the magnitude of an unknown transverse field can be unambiguously identified through the measurement of the signal curvature. The angular orientation can be determined up to a two-fold degeneracy by observing the change in signal curvature produced when the bias field is shifted off-axis.

Thesis Supervisor: =====

=====

## CONTENTS

1	Introduction	6
2	Background	7
2.1	Spin Structure of the Nitrogen-Vacancy Defect . . . . .	7
2.2	Detection of Magnetic Fields with the NV Center . . . . .	8
2.3	The All-Optical Method of NV Magnetometry . . . . .	9
2.4	Non-degenerate Time-Independent Perturbation Theory (Non-degenerate TIPTD) . . . . .	10
2.5	The Seven-Level Model of the NV Spin Level Structure . . . . .	10
3	Model Details	11
3.1	Calculation of $\alpha_{ij}$ via Non-degenerate TIPT . . . . .	12
3.2	Numerical Details of the Transition Rates . . . . .	13
3.3	Reformulation of the Model Equations as a Linear Matrix System . . . . .	14
3.4	Extension to Ensembles . . . . .	15
4	Detection of Magnetic Fields	18
4.1	Parallel Fields . . . . .	18
4.2	Transverse Fields . . . . .	20
5	Conclusion	28
5.1	Future Work to Be Explored . . . . .	28
6	Appendix	29
6.1	Approximate Nullspace of $M$ . . . . .	29
6.2	Noise Model . . . . .	30

## LIST OF FIGURES

Figure 1	The seven level model in the absence of an external magnetic field, consisting of the ground state and excited state triplets and a metastable singlet. Only spin-conserving radiative transitions and non-radiative transitions to the metastable state are considered. . . . .	7
Figure 2	A depiction of the Zeeman splitting of the triplet ground state. . . . .	8
Figure 3	The normalized PL intensity as a function of the transverse magnetic field amplitude. The parallel projection onto the defect axis is held constant at $B_z = .03T$ . . . . .	9
Figure 4	(Left) The tetrahedral geometry to be considered. The tetrahedral angle is $109.5^\circ$ and $\rho$ is the angle between $\vec{B}$ and $\hat{z}$ . (Right) The tetrahedral geometry projected into the transverse plane. The angle of symmetry is $120^\circ$ and $\beta$ is the offset of the tetrahedron with the x-axis, which is defined along the transverse field component. . . . .	16
Figure 5	Rotation profiles of the observed signal within the x-y plane. $\rho$ , the angle between $\vec{B}$ and $\hat{z}$ , increases from top to bottom from $20^\circ$ to $85^\circ$ to $90^\circ$ . For all, $ B  = .03T$ and $\Gamma$ is set to 10. The intensities are normalized to the $\rho = 0^\circ$ intensities. . . . .	17

Figure 6	A full $4\pi$ rotation map of the NV tetrahedron. $\rho$ is the polar angle of the external magnetic field and $\beta$ is the azimuthal angle. $ B $ is .01T and $\Gamma$ is set to 10. . . . .	18
Figure 7	A demonstration of the increased sensitivity of the NV center to perturbing transverse fields around the LAC regions $\sim .05T$ and $\sim .1T$ . On the left is the single NV case, while on the right the full ensemble is considered. Circled are the 3 symmetry points about which a perturbing parallel field could be readily identified with the methods discussed in the text. $\Gamma = 10$ in both cases. The small deviations that occur near the LAC points are due to divergences in the coefficients $\alpha_{ij}$ that develop as a manifestation of the Perturbation Theory and are not physical. . . . .	19
Figure 8	The geometry of the perturbing magnetic field. $\Psi$ is the angle between the perturbing field and the z-axis, and $\Omega$ is the angle between the perturbing field and the x-axis. . . . .	21
Figure 9	A plot demonstrating the effect of the transverse field on the observed signal when the system is biased around the excited state LAC. Clearly the observed signal approaches a steady value for $B_x \gtrsim .002T$ . In generating this plot $B_z = .05T$ and $\Gamma = 10$ . . . . .	22
Figure 10	A series of plots depicting the dependencies of the signal curvature on $B_x$ (Top), $\beta$ (Middle) and $\Gamma$ (Bottom). Clearly, a change in the transverse field magnitude is the dominant cause for changes in the observed signal curvature. It is therefore proposed that by monitoring the changes in the signal curvature the transverse perturbation magnitude can be determined.	23
Figure 11	(Blue) A plot of the curvature of the signal profile evaluated at $B_z = .052T$ and $\Gamma = 10$ as a function of $B_x$ . (Green) A fitted curve $\left. \frac{\partial^2 S}{\partial B_x^2} \right _{.052} = \frac{586038}{(B_x - .0005T)^2}$ to extract the leading order dependence of the signal curvature upon $B_x$ . . . . .	24
Figure 12	The rotational symmetry of the total transverse field (red). The dotted circle represents the projections of equal $B_{\perp}$ and is what would be observed experimentally. For a fixed transverse bias field $B_{\perp}^0$ (black), any transverse perturbing field $b_{\perp}$ (blue) that creates a $B_{\perp}$ with the observed magnitude is an allowable solution due to the rotational invariance of the signal curvature. For the case $ a  \geq 1$ there is one positive solution for $b_{\perp}$ for all values of $\Omega$ in the range $[0, 2\pi]$ . For the case $ a  = 1$ there is one positive solution for $b_{\perp}$ for all values of $\Omega$ in the range $[\frac{\pi}{2}, \frac{3\pi}{2}]$ . For the case $ a  < 1$ there are only positive solutions for $b_{\perp}$ for the negative angle interval when $ \sin \Omega  \leq  a $ . Usually there are 2 possible solutions on this interval, but when $ \sin \Omega  =  a $ there is only one tangent solution. . . . .	25

## LIST OF TABLES

Table 1	The rate values used in the calculations presented in this thesis. All transition rates not shown are taken to be 0. . . . .	14
Table 2	The parallel and perpendicular projections of an external magnetic field $\vec{B} = B_x\hat{x} + B_z\hat{z}$ onto the 4 possible defect axes. The angles $\theta_0$ , $\beta$ and $\varphi_0$ are defined in the text. . . . .	16

## 1 INTRODUCTION

The accurate measurement of magnetic fields at small scales can be beneficial for a variety of scientific endeavors. For example, measuring the magnetic field produced by nuclear spins of a protein with high spatial resolution can yield information regarding its molecular structure[1–3], and dynamic imaging can reveal the manner in which proteins fold and unfold[4–8]. Furthermore, intracellular processes and mechanisms can be better studied by monitoring the distribution and evolution of magnetic moments within the cell[9–14], with better spatial resolution yielding better understanding. The currently used methods of small scale magnetometry, superconducting quantum interference devices[15–17], atomic vapor based magnetometry[18,19], and magnetic resonance force microscopy[20–22], are either not capable of resolving changes on a nanometer scale, or require difficult operational procedures, such as cryogenic temperatures or large sample sizes, which are not suitable in certain contexts. Thus for high precision measurements that are to be performed in ambient conditions, a new method of magnetometry is necessary.

A suitable candidate is the Nitrogen-Vacancy defect in diamond, which promises nanoscale precision even when operated at room temperature[23, 24]. A NV center occurs when a nitrogen substitutional defect is located next to a vacancy in the lattice structure, which can occur naturally or can be induced through laboratory methods[25–29]. Of interest to this project is the  $NV^-$  center<sup>1</sup>, in which an additional electron is located within the defect site.

The NV center is known as a color center because it will fluoresce within the visible spectrum when optically excited. As will be discussed in more detail, the intensity of the emitted light is intimately related to the spin state of the NV center, and because quantum spins interact with magnetic fields in a well-understood manner, by monitoring changes in the intensity of the NV center fluorescence emission, the local magnetic field profile can be reconstructed.

In this work, we develop a method of NV magnetometry known as the all-optical method[30, 31] analytically and numerically, and ultimately extend this model to include the effect of ensembles of NV centers rather than a single defect center. In Section II we introduce the relevant features of the NV center, and present the motivation for the all-optical technique as a consequence of the Zeeman interactions between the NV spin structure and the external magnetic field. We introduce the model equations as well. In Section III we develop the model equations in more detail and modify them to be more convenient for computational analysis. Finally, section IV presents the results of the solved model equations and discusses the implications of the results on future experimental implementations of the all-optical method of NV magnetometry.

---

<sup>1</sup> Henceforth, the  $NV^-$  center will be referred to simply as the NV center

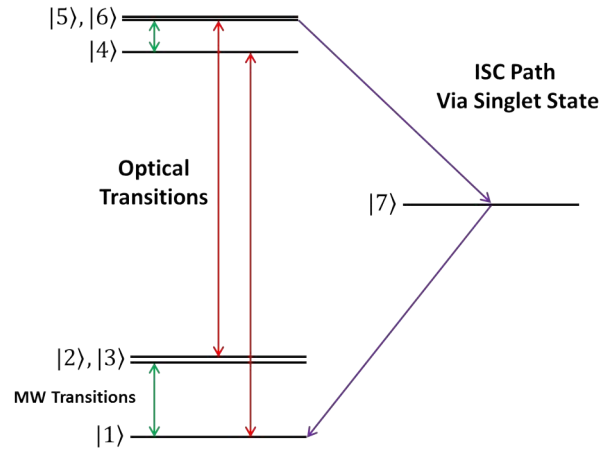


**Figure 1:** The seven level model in the absence of an external magnetic field, consisting of the ground state and excited state triplets and a metastable singlet. Only spin-conserving radiative transitions and non-radiative transitions to the metastable state are considered.

## 2 BACKGROUND

### 2.1 Spin Structure of the Nitrogen-Vacancy Defect

The ground state of this system is a spin-1 triplet. There is a zero-field splitting of the triplet state of 2.87 GHz due to spin-spin interactions that places the  $|0\rangle$  state below the  $|\pm\rangle$  states. This triplet ground state can be excited with 532 nm wavelength laser light into an excited triplet state with 1.42 GHz zero-field splitting<sup>2</sup>. The subsequent relaxation process will yield an amount of photons dependent upon the relaxation path.

The dominant mode of relaxation is through spin-conserving transitions[32, 33]; for example, a state belonging to the excited state manifold will transition to its equivalent spin state in the ground state manifold, emitting a photon in the process to satisfy overall energy conservation. However, the total number of photons emitted after repeated optical stimulations is highly dependent upon the initial polarization of the state[34, 35]. This is due to the finite probability that the  $|\pm\rangle$  states will transition to the  $|0\rangle$  state via a metastable singlet state<sup>3</sup>, a process known as intersystem crossing (ISC). This transition excites phonons in place of photons, so on average the observed number of photons emitted by the  $|\pm\rangle$  states is less than that of the  $|0\rangle$  state. Fig. 1 gives a visual representation to the electronic and spin level structure of the NV defect.

<sup>2</sup> It is the preservation of this unique spin level structure at room temperatures that allows NV magnetometry to be operable in ambient conditions

<sup>3</sup> Note: the opposite phenomenon, the excited  $|0\rangle$  state transitioning to a  $|\pm\rangle$  state via the metastable state, is negligible compared to the probability of radiative decay.

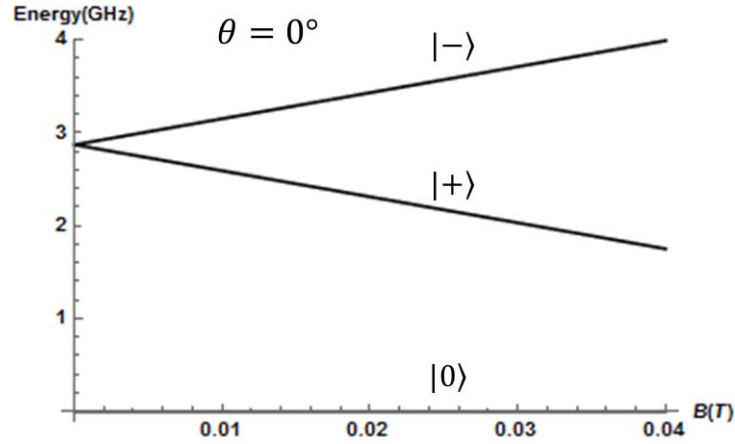
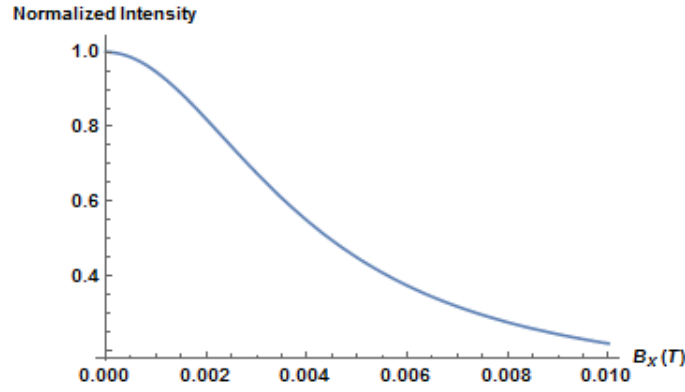


Figure 2: A depiction of the Zeeman splitting of the triplet ground state.

## 2.2 Detection of Magnetic Fields with the NV Center

It is well known that spins interact with external magnetic fields through what is known as the Zeeman Effect, where spins aligned with the magnetic field will occupy a lower energy state than spins anti-aligned to it. In particular for the spin-1 triplet state of the NV defect and a magnetic field aligned with the defect axis, the energy of the  $|+\rangle$  state is shifted downward by the amount  $\mu g B \approx (11.6 \text{ eV/T}) \cdot B$ , the energy of the  $|-\rangle$  is shifted upward by the same amount and the energy of the  $|0\rangle$  state is unaffected, as can be seen in Fig. 2. Experimentally, this splitting can be observed by performing microwave (MW) sweeps while optically exciting the NV center and observing the PL decrease when the MW is resonant with the  $|0\rangle \rightarrow |\pm\rangle$  transition at the applied magnetic field[36,37].

Monitoring the electron spin resonance (ESR) spectra of the NV center provides a method of extracting the magnitude of the external magnetic field projected onto the defect axis due to the known relation between the energy splitting and the external magnetic field; however, this detection method is insensitive to transverse fields. Similarly, another method of NV magnetometry is the use of a Ramsey-type pulse sequence for DC fields and Spin-echo[38–41] measurements for AC fields. These methods consists of a  $\frac{\pi}{2}$  resonant MW pulse followed by a period of free evolution in which the  $|\pm\rangle$  states will pick up a phase due to their interaction with the external magnetic field, followed by a final  $\frac{\pi}{2}$  MW pulse which projects the state back onto the original axis. This final pulse effectively translates the phase difference obtained during the period of free evolution (which is proportional to the magnetic field) to a measurable difference in spin state populations. An additional  $\pi$  pulse is inserted in the middle of the echo sequence that will "flip" the state and the direction of the spin evolution, allowing the phase difference to continue to increase even as the external field magnetic field changes sign. However, these pulse sequences will be insensitive to transverse fields as well. Therefore, a third method of NV magnetometry, known as the all-optical method, is now introduced that is capable of directly detecting the presence of a transverse magnetic field.



**Figure 3:** The normalized PL intensity as a function of the transverse magnetic field amplitude. The parallel projection onto the defect axis is held constant at  $B_z = .03\text{T}$ .

### 2.3 The All-Optical Method of NV Magnetometry

In the absence of continuous or pulsed MW driving, an aligned magnetic field will cause no changes in the photoluminescence (PL) intensity as its magnitude is increased; the same, however, is not true for transverse fields. In strong transverse fields, the  $m_s$  basis with respect to the spin axis is not a good eigenbasis in which to analyze the system; instead, an eigenbasis with respect to the axis of the magnetic field would serve better[42]. Eigenstates in this new basis can be expressed as superpositions of the previous  $m_s$  states and as a consequence there will be a nonzero overlap between the  $|0\rangle$  in the new basis and the  $|m_s = \pm\rangle$  of the old basis. Through this effect, the contrast in photons emitted by the  $|0\rangle$  and the  $|\pm\rangle$  states is reduced; however the net intensity of the photon light is also reduced due to the larger population of  $|\pm\rangle$  states (see Fig. 3). While this behavior is intuitive for the case of a strong transverse field, this reduction in PL intensity will be manifested even in the regime of small transverse fields as long as the transverse field is nonzero. It may therefore be possible to detect the presence of transverse fields by monitoring a change in the intensity of emitted light.

For a single NV center, this approach is strictly limited to the detection of transverse fields. However for ensembles of NV centers this limitation is removed. The diamond lattice has a face-centered cubic structure; correspondingly, there are four possible spatial orientations for the NV defect[43]. An external magnetic field parallel to one NV center will be at an angle to another NV center within the sample. Therefore, when considering ensembles of NV centers, the all-optical method of magnetometry can be used for the successful detection of magnetic fields of any orientation.

An ongoing field of research is the use of the NV center to make precision measurements of a small-scale magnetic field; however, with the increased precision comes an expected decrease in simplicity of experimental design. The methods developed in this thesis project aim to accomplish the opposite: a relatively quick and simple method of detecting small-scale magnetic fields at the expense of decreased precision in the measurement. The results of this project can be used to develop a tool for performing fast measurements when the ultimate sensitivity is not the primary concern (although nanoscale precision is still obtainable, even with such an "imprecise" device), or an apparatus that can be used in tabletop demonstrations in either labora-

tory settings or a presentation to a general audience, since the measurement methods will be simple to perform.

#### 2.4 Non-degenerate Time-Independent Perturbation Theory (Non-degenerate TIPD)

Perturbative analysis is useful for systems in which small changes are made to an exactly-solvable unperturbed Hamiltonian, as is the case with the interaction of an external magnetic field with the NV defect. The total eigenstates and eigenvalues are then expanded in a power series around the small perturbation and truncated at an appropriate order. That is to say, we begin with an unperturbed Hamiltonian  $H_0$  with unperturbed eigenstates  $|n^0\rangle$  such that

$$H_0 |n^0\rangle = E_n^0 |n^0\rangle \quad (1)$$

A small perturbation is added to the original Hamiltonian such that

$$H_{\text{tot}} = H_0 + \delta H \quad (2)$$

where  $\delta H$  is small compared to  $H_0$ . The eigenvalues then evolve according to the equation:

$$E_n = E_n^0 + \langle n^0 | \delta H | n^0 \rangle + \sum_{m \neq n} \frac{|\langle m^0 | \delta H | n^0 \rangle|^2}{E_n^0 - E_m^0} + \dots \quad (3)$$

Similarly, the eigenstates will evolve according to the equation:

$$|n\rangle = |n^0\rangle + \sum_{m \neq n} \frac{\langle m^0 | \delta H | n^0 \rangle}{E_n^0 - E_m^0} |m^0\rangle + \dots \quad (4)$$

These results will be used in the next section to calculate the Zeeman interaction for the NV defect.

#### 2.5 The Seven-Level Model of the NV Spin Level Structure

The seven level model is defined such that the zero field states  $\{|i\rangle\}$  form a complete basis. Therefore, the new states that result from the application of the external magnetic field (denoted as  $|i'\rangle$ ) can be expressed as a linear combination of the original states[30]:

$$|i'\rangle = \sum_{j=1}^7 \alpha_{ij}(B) |j\rangle \quad (5)$$

where the coefficients  $\alpha_{ij}(B)$  will be determined via Perturbation Theory (PT) in the following section and are functions of the external magnetic field.

Transition rates are represented as  $k_{ij}$  for the transition  $|i\rangle \rightarrow |j\rangle$ . In a similar manner to Eq. 5, the new relaxation rates (denoted as  $k'_{ij}$ ) will evolve as combinations of the zero-field transition rates[30]:

$$k'_{ij} = \sum_{p,q=1}^7 |\alpha_{ip}|^2 |\alpha_{jq}|^2 k_{pq} \quad (6)$$

In the most general case, the time evolution of the spin state populations can be calculated with the classical rate equations[30]:

$$\frac{dn_i}{dt} = \sum_{j=1}^7 k'_{ji} n_j - k'_{ij} n_i \quad (7)$$

However, for the purposes of the all-optical measurement approach, the above equation will be solved in the steady-state condition with  $\frac{d}{dt} \rightarrow 0$ . Physically, this corresponds to an experimental setup in which the NV center is optically excited long enough for transient behavior to diminish, and then photon collection will occur while the NV center is continuously illuminated such that the steady-state condition is maintained for the entirety of the measurement period. Thus, the equation to be solved is:

$$0 = \sum_{i,j=1}^7 k'_{ji} \bar{n}_j - k'_{ij} \bar{n}_i \quad (8)$$

where the spin state populations are denoted as  $\bar{n}_i$  to indicate they are the steady-state populations. The spin populations represent the probabilities for a single NV center to be in the specified spin state, thus the following normalization condition is imposed on  $\{\bar{n}_i\}$ [30]:

$$\sum_{i=1}^7 \bar{n}_i = 1 \quad (9)$$

Recall that the decay of the excited state manifold to the ground state manifold via the metastable state excites phonon production rather than photon emission, thus the only radiative decays are those from the excited state manifold directly to the ground state manifold. Thus the rate of total radiative decay,  $R$ , is defined with the following equation[30]:

$$R = \eta \sum_{i=4}^6 \sum_{j=1}^3 k'_{ij} \bar{n}_i \quad (10)$$

where  $\eta$  represents the collection efficiency of the photon detector.

### 3 MODEL DETAILS

In the seven-level model the complete Hilbert space will be decomposed into 3 independent subspaces - the ground state manifold, with the basis  $\{|1\rangle, |2\rangle, |3\rangle\}$ , the excited state manifold, with the basis  $\{|4\rangle, |5\rangle, |6\rangle\}$ , and the metastable singlet  $\{|7\rangle\}$ . In this manner the Hamiltonians of each subspace may be considered independently as well, as the total Hamiltonian will be of simple block-diagonal form. This will simplify the calculations, because the singlet will exhibit no Zeeman interactions, and the evolution of the excited state manifold due to the external magnetic field will be analogous to that of the ground state manifold. The dimensionality of the problem can thus be reduced from 7 to 3 by limiting the analysis to the calculation of the Zeeman interactions of the ground state manifold only. Furthermore, the subspace independence implies that there will be no state mixing between subspaces, and as such the amount of coefficients  $\alpha_i$  is greatly reduced.

Defining the quantization axis to lie along the NV defect axis, the ground state Hamiltonian is thus composed of two terms<sup>4</sup>:

$$H_{gs} = \hbar D_{gs} S_z^2 - \mu g \vec{B} \cdot \vec{S} \quad (11)$$

where only the zero-field splitting of the ground state manifold and the Zeeman interaction with the external magnetic field are considered. Here,  $\hbar$  is the Planck constant,  $\mu$  is the Bohr magneton and  $D_{gs} = 2.87\text{GHz}$ . The analogous excited state Hamiltonian can be found by replacing  $D_{gs}$  with  $D_{es} = 1.42\text{GHz}$ .

When considering a single NV center, the transverse field can be taken to lie along the x-axis without loss of generality. However, we are interested in performing our analysis in the most general way and in particular in extending it to ensemble of NVs, oriented along the four different crystal axes. We thus initially retain the most general form of the Hamiltonian. This allows us to show that even in the most general case the problem can still be reduced to a 2-parameter model, defined by a longitudinal and transverse magnetic field. Thus, the ground state Hamiltonian is:

$$H_{gs} = \hbar D_{gs} S_z^2 - \mu g B_z S_z - \mu g B_x S_x - \mu g B_y S_y \quad (12)$$

### 3.1 Calculation of $\alpha_{ij}$ via Non-degenerate TIPT

For small transverse fields ( $\frac{\mu g B_{\perp}}{\hbar D_{gs}} \ll 1$ ) the effect of the transverse field on the spin eigenstates can be calculated via Time Independent Perturbation Theory. The total Hamiltonian of the system is decomposed as follows:

$$H_{\text{tot}} = H_0 + \delta H \quad (13)$$

with the unperturbed and perturbing Hamiltonians defined as

$$\begin{aligned} H_0 &= H_{gs} = \hbar D_{gs} S_z^2 - \mu g B_z S_z \\ \delta H &= -\mu g B_x S_x - \mu g B_y S_y \end{aligned} \quad (14)$$

The unperturbed eigenvalues are the usual  $S_z$  eigenvalues  $|-\rangle, |0\rangle, |+\rangle$ .

The presence of a finite  $B_z$  breaks the degeneracy of the states  $|\pm\rangle$  and thus Non-degenerate PT can be used. Applying Eq. 3 with the given definitions of  $H_0$  and  $\delta H$  the new energies are found to be:

$$\begin{aligned} E_+ &= \hbar D_{gs} - \mu g B_z + \frac{(\mu g)^2 |B_x + iB_y|^2}{2(\hbar D_{gs} - \mu g B_z)} + \dots \\ E_0 &= -\frac{(\mu g)^2 |B_x - iB_y|^2}{2(\hbar D_{gs} - \mu g B_z)} - \frac{(\mu g)^2 |B_x + iB_y|^2}{2(\hbar D_{gs} + \mu g B_z)} + \dots \\ E_- &= \hbar D_{gs} + \mu g B_z + \frac{(\mu g)^2 |B_x - iB_y|^2}{2(\hbar D_{gs} + \mu g B_z)} + \dots \end{aligned} \quad (15)$$

<sup>4</sup> For reference, the spin-1 operators, in the  $S_z$  eigenbasis, are:

$$S_x = \begin{pmatrix} 0 & \frac{1}{\sqrt{2}} & 0 \\ \frac{1}{\sqrt{2}} & 0 & \frac{1}{\sqrt{2}} \\ 0 & \frac{1}{\sqrt{2}} & 0 \end{pmatrix}, S_y = \begin{pmatrix} 0 & \frac{-i}{\sqrt{2}} & 0 \\ \frac{i}{\sqrt{2}} & 0 & \frac{-i}{\sqrt{2}} \\ 0 & \frac{i}{\sqrt{2}} & 0 \end{pmatrix}, S_z = \begin{pmatrix} 1 & 0 & 0 \\ 0 & 0 & 0 \\ 0 & 0 & -1 \end{pmatrix}$$

and applying Eq. 4 the new eigenstates are found to be:

$$\begin{aligned}
|+\rangle &= |+\rangle - \frac{\mu g(B_x + iB_y)}{\sqrt{2}(\hbar D_{gs} - \mu g B_z)} |0^0\rangle + \dots \\
|0\rangle &= |0^0\rangle + \frac{\mu g(B_x - iB_y)}{\sqrt{2}(\hbar D_{gs} - \mu g B_z)} |+\rangle + \frac{\mu g(B_x + iB_y)}{\sqrt{2}(\hbar D_{gs} + \mu g B_z)} |-\rangle + \dots \\
|-\rangle &= |-\rangle - \frac{\mu g(B_x - iB_y)}{\sqrt{2}(\hbar D_{gs} + \mu g B_z)} |0^0\rangle + \dots
\end{aligned} \tag{16}$$

Generally, the new eigenstates should be renormalized, however in this case the perturbation will be considered to be sufficiently small that the eigenvectors remain approximately normalized. The physical quantities of interest for this system are the energies of the states  $E_i$  and the norm-squared coefficients  $|\alpha_{ij}|^2$ . From the above expressions it is clear that both quantities depend on the magnitude of the transverse field component ( $B_{\perp}^2 \equiv B_x^2 + B_y^2$ ) without regard for the orientation of the transverse field in the x-y plane. Therefore, for every NV center to be considered, the relevant field quantities are  $B_{\parallel}$  and  $B_{\perp}$  and all formulas derived shall be written in terms of these 2 quantities such that the generalization to ensembles is manifestly visible.

From Eq. 16, the coefficients  $\alpha_{ij}$  can be easily identified, recalling the mapping of  $|0\rangle \rightarrow |1\rangle, |+\rangle \rightarrow |2\rangle, |-\rangle \rightarrow |3\rangle$ . For completeness all non-zero  $\alpha_{ij}$  coefficients are listed here:

$$\begin{aligned}
\alpha_{11} &= 1 & \alpha_{44} &= 1 \\
\alpha_{12} &= \frac{\mu g B_{\perp}}{\sqrt{2}(\hbar D_{gs} - \mu g B_{\parallel})} & \alpha_{45} &= \frac{\mu g B_{\perp}}{\sqrt{2}(\hbar D_{es} - \mu g B_{\parallel})} \\
\alpha_{13} &= \frac{\mu g B_{\perp}}{\sqrt{2}(\hbar D_{gs} + \mu g B_{\parallel})} & \alpha_{46} &= \frac{\mu g B_{\perp}}{\sqrt{2}(\hbar D_{es} + \mu g B_{\parallel})} \\
\alpha_{21} &= -\frac{\mu g B_{\perp}}{\sqrt{2}(\hbar D_{gs} - \mu g B_{\parallel})} & \alpha_{54} &= -\frac{\mu g B_{\perp}}{\sqrt{2}(\hbar D_{es} - \mu g B_{\parallel})} \\
\alpha_{22} &= 1 & \alpha_{55} &= 1 \\
\alpha_{31} &= -\frac{\mu g B_{\perp}}{\sqrt{2}(\hbar D_{gs} + \mu g B_{\parallel})} & \alpha_{64} &= -\frac{\mu g B_{\perp}}{\sqrt{2}(\hbar D_{es} + \mu g B_{\parallel})} \\
\alpha_{33} &= 1 & \alpha_{66} &= 1 \\
\alpha_{77} &= 1
\end{aligned} \tag{17}$$

### 3.2 Numerical Details of the Transition Rates

In this model only spin-conserving radiative transitions and ISC transitions via the metastable singlet state are considered. The metastable state is assumed to only couple with the ground state  $|0\rangle$  and the excited state  $|\pm\rangle$ . Furthermore, the transition rates depend only on the absolute value of  $m_s$ , so transition rates involving the  $|+\rangle$  and  $|-\rangle$  states will be equal. Table 1 shows the exact numerical values used in developing the results presented in this thesis[32].

Excitation rates ( $k_{ji}$ ,  $i \in \{1, 2, 3\}$ ,  $j \in \{4, 5, 6\}$ ) can be related to the corresponding relaxation rates with a constant of proportionality  $\Gamma_{ij}$  known as the optical pumping parameter for that transition. In general  $\Gamma_{ij}$  is different

Transition	Rate [MHz]
$k_{41}$	77
$k_{52}$	77
$k_{63}$	77
$k_{57}$	30
$k_{67}$	30
$k_{71}$	3.3

**Table 1:** The rate values used in the calculations presented in this thesis. All transition rates not shown are taken to be 0.

for the different radiative decay processes. However, in this model only spin-conserving radiative transitions are considered, and as can be seen in Table 1 these transition rates are all equal. The laser excitation process can similarly be considered independent of the initial spin polarization, and thus the ratio  $\Gamma_{ij} = k_{ji}/k_{ij} \equiv \Gamma$  is a constant of the experiment.

### 3.3 Reformulation of the Model Equations as a Linear Matrix System

To simplify the analysis, it is desired to reformulate the model equations (Eqs. 6 - 10) as matrix equations in order to reduce the overall number of equations to be solved directly. The evolution of the basis states (Eq. 5) does not aim to benefit from any reformulation, as the new basis states have already been calculated via Perturbation Theory and can thus be directly operated on in place of the original basis states. Therefore we began with Eq. 6.

The matrix  $A$  is defined such that:

$$A \equiv |\alpha_{ij}|^2 |i\rangle \langle j| \quad (18)$$

Furthermore, the matrices  $K$  and  $K'$  are defined such that:

$$\begin{aligned} K &\equiv k_{ij} |i\rangle \langle j| \\ K' &\equiv k'_{ij} |i\rangle \langle j| \end{aligned} \quad (19)$$

With these definitions, it is clear to see that Eq. 6 can be reformulated as:

$$K' = AKAT \quad (20)$$

It should be noted that the above equation is valid for any choice of  $A$ ; however, from Eq. 17 it can be seen the  $A$  derived for this system is symmetric, and as such  $A$  and  $A^T$  will be equivalent. In fact, when only considering the first order correction to the basis states obtained via Perturbation Theory (Degenerate or Non-degenerate), the hermiticity of the Hamiltonian implies  $A$  will be always symmetric.

In reformulating Eq. 8 we define the vector  $|n\rangle$  such that each element of the vector is the steady-state probability  $\bar{n}_i$  as defined in Eq. 9. Upon inspection of Eq. 8, it is clear that there are two types of terms present: the first is a sum of the possible decays into the spin state of interest, which is dependent upon the other spin populations, while the second is a sum of all the possible decays out of the spin state of interest and is independent

of the populations of the other spin states. With this recognized, it follows that Eq. 8 can be alternatively expressed as<sup>5</sup>:

$$\begin{aligned}\vec{0} &= (\mathbf{K}' - \text{Diag}(\mathbf{K}'|\mathbf{I}))^T |\mathbf{n}\rangle \\ &= \mathbf{M} |\mathbf{n}\rangle\end{aligned}\quad (21)$$

The first term in  $\mathbf{M}$  represents the decays into a spin state, while the second term represents the decays out of a spin state. In this representation, solving for the steady-state spin populations is recast as the problem to find the nullspace of  $\mathbf{M}$ , which is a well-studied problem<sup>6</sup>.

With this approach, the normalization condition of  $\vec{n}$  is alternatively expressed as:

$$\langle \mathbf{n} | \mathbf{1} \rangle = 1 \quad (22)$$

To recast Eq. 10 into a matrix equation, for brevity in the final result the vector  $|G\rangle$  and the matrix  $\mathbf{E}$  are defined as:

$$\begin{aligned}|G\rangle &\equiv |1\rangle + |2\rangle + |3\rangle \\ \mathbf{E} &\equiv |4\rangle \langle 4| + |5\rangle \langle 5| + |6\rangle \langle 6|\end{aligned}\quad (23)$$

It is clear that the total radiative rate can then be expressed as:

$$\mathbf{R} = \eta \langle \mathbf{n} | \mathbf{E} \mathbf{K}' | G \rangle \quad (24)$$

### 3.4 Extension to Ensembles

When considering an ensemble of NV centers, there exists a potential ambiguity in distinguishing angular and gradient effects in the total observed PL signal. A more complete analysis of the system would allow for a spatially-varying external field; however, for simplicity the external field will be assumed to be slowly varying over the ensemble region ( $\frac{\sqrt{\nabla|B|}}{B_{\text{ave}}} \ll 1$ ). This work will focus on the leading order term only, but corrections due to small spatial variations can be added in a Taylor expansion of the signal calculation.

As discussed in the previous section, the response of the NV center to an external magnetic field can always be treated as a 2-dimensional problem with the relevant parameters being  $B_{\parallel}$  and  $B_{\perp}$ , the parallel and transverse projections of the external field onto the defect axis respectively. In calculating  $B_{\parallel}$  and  $B_{\perp}$ , however, the full 3-dimensionality of the diamond lattice must be maintained. Symmetry considerations dictate the diamond lattice to be tetrahedral. Defining the coordinate axes such that  $\hat{z}$  lies along one of the bond axes (hereby denoted as  $\hat{P}$  for Principle Axis<sup>7</sup>) and  $\hat{x}$  lies along the transverse field direction, it is straightforward to calculate the parallel and perpendicular projections of  $\vec{B}$  on the other 3 bond axes (hereby denoted as  $\hat{Q}$ ,  $\hat{R}$ ,  $\hat{S}$ <sup>8</sup>); the results are shown in Table 2. In calculating the results of Table 2, the following angles are defined:  $\theta_0 \approx 109.5^\circ$  is the bond angle,  $\beta$  is the angle between the transverse axis projection  $\hat{Q}_{\perp}$  and the transverse field

<sup>5</sup> Notation:  $\vec{0}$  is the seven dimensional all-zeros vector (0 0 0 0 0 0 0),  $|\mathbf{I}\rangle$  is the seven dimensional all-ones vector  $\sum |\mathbf{i}\rangle$ ,  $\text{Diag}(\vec{\alpha})$  defines the matrix  $\mathbf{D}$  such that  $D_{ij} = \alpha_i \delta_{ij}$ , where  $\delta_{ij}$  is the Kronecker Delta.

<sup>6</sup> Note that with this representation the transient case becomes similarly recast into a well-studied form:  $\dot{\vec{n}} = \mathbf{M}\vec{n}$

<sup>7</sup> Note: All such references to “parallel” and “transverse” projections should be understood to be taken with respect to the Principle Axis

<sup>8</sup> Alternatively, one can consider the representations  $\hat{P} \rightarrow (111)$ ,  $\hat{Q} \rightarrow (1\bar{1}\bar{1})$ ,  $\hat{R} \rightarrow (\bar{1}1\bar{1})$ ,  $\hat{S} \rightarrow (\bar{1}\bar{1}1)$

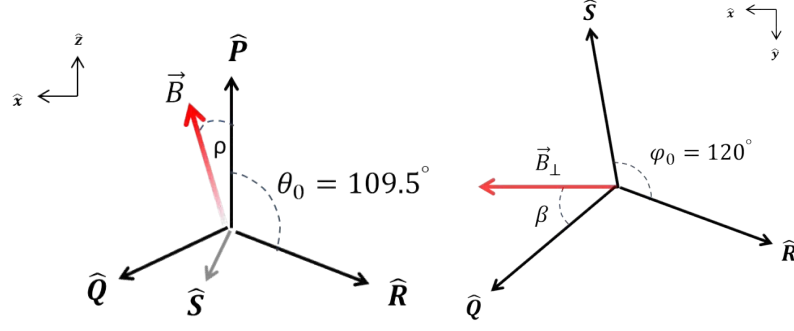


**Figure 4:** (Left) The tetrahedral geometry to be considered. The tetrahedral angle is  $109.5^\circ$  and  $\rho$  is the angle between  $\vec{B}$  and  $\hat{z}$ . (Right) The tetrahedral geometry projected into the transverse plane. The angle of symmetry is  $120^\circ$  and  $\beta$  is the offset of the tetrahedron with the  $x$ -axis, which is defined along the transverse field component.

	$ B_\parallel $	$ B_\perp $
$\hat{P}$	$B_z$	$B_x$
$\hat{Q}$	$B_x \sin \theta_0 \cos \beta + B_z \cos \theta_0$	$\sqrt{B^2 - (B_x \sin \theta_0 \cos \beta + B_z \cos \theta_0)^2}$
$\hat{R}$	$B_x \sin \theta_0 \cos(\beta + \varphi_0) + B_z \cos \theta_0$	$\sqrt{B^2 - (B_x \sin \theta_0 \cos(\beta + \varphi_0) + B_z \cos \theta_0)^2}$
$\hat{S}$	$B_x \sin \theta_0 \cos(\beta - \varphi_0) + B_z \cos \theta_0$	$\sqrt{B^2 - (B_x \sin \theta_0 \cos(\beta - \varphi_0) + B_z \cos \theta_0)^2}$

**Table 2:** The parallel and perpendicular projections of an external magnetic field  $\vec{B} = B_x \hat{x} + B_z \hat{z}$  onto the 4 possible defect axes. The angles  $\theta_0$ ,  $\beta$  and  $\varphi_0$  are defined in the text.

direction,  $\varphi_0 = 120^\circ$  is the angular spacing of the three axes projections in the  $x$ - $y$  plane. Fig. 4 provides a visual representation of this coordinate configuration.

As can be clearly seen in Table 2, at most 3 tetrahedral axes can be considered symmetrically, in which the parallel and perpendicular projections of the external field will be equal. In this coordinate system this occurs when  $B_x = 0$ . These coordinates were chosen to make this feature manifest but no generality was lost in this coordinate definition - there does not exist an external field orientation in which the parallel or perpendicular projections onto every tetrahedral axis are identical. The most symmetric configuration will always be when the external field is perfectly aligned with a tetrahedral axis.

With the projections defined, the total signal observed is a simple average over the 4 possible orientations with the assumption that the interactions between neighboring NV centers can be neglected. Thus:

$$\bar{S} = \frac{1}{4} \sum_{\hat{n}} R(B_\parallel^{\hat{n}}, B_\perp^{\hat{n}}) \quad (25)$$

where  $\hat{n} = \hat{P}, \hat{Q}, \hat{R}, \hat{S}$ .

Due to the trifold rotational symmetry of this geometry, a periodic signal profile develops in the presence of a finite transverse field, as can be seen in Fig. 5. Interestingly, in the quasi-parallel regime, in which  $B_x \ll B_z$ , the signal peaks occur when the tetrahedral axes are anti-aligned with the transverse field. This is due to the bond angle being obtuse, so in the quasi-parallel regime a transverse field anti-aligned with a transverse tetrahedral

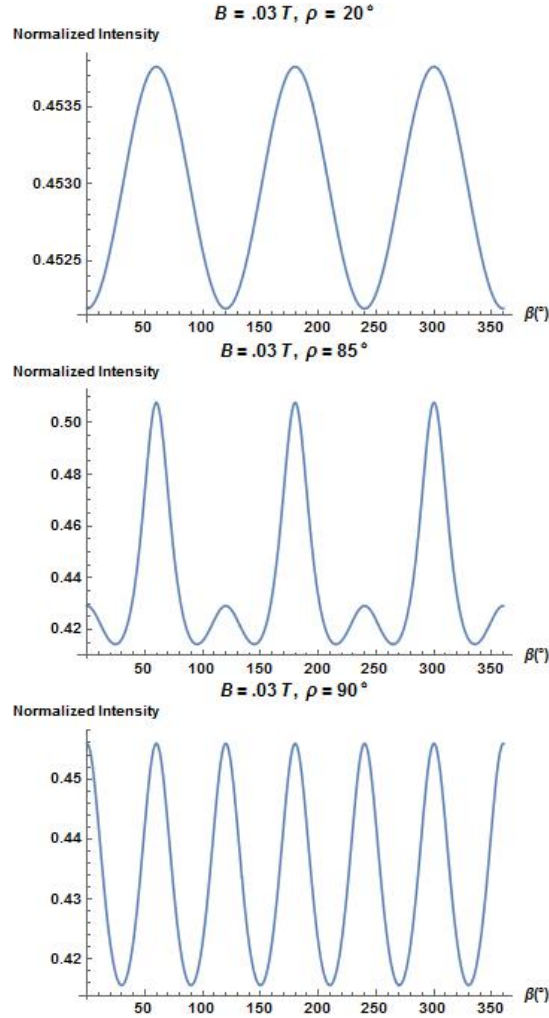


Figure 5: Rotation profiles of the observed signal within the x-y plane.  $\rho$ , the angle between  $\vec{B}$  and  $\hat{z}$ , increases from top to bottom from  $20^\circ$  to  $85^\circ$  to  $90^\circ$ . For all,  $|\vec{B}| = .03T$  and  $\Gamma$  is set to 10. The intensities are normalized to the  $\rho = 0^\circ$  intensities.

axis has a larger parallel projection onto that axis than when aligned with it. As the system is rotated into the quasi-transverse regime, in which  $B_x \gg B_z$ , the aligned configurations transition from local minima to local maxima as the minima shift towards the midpoint between the aligned and anti-aligned configurations. Finally, for completely transverse fields the aligned and anti-aligned configurations are perfectly symmetric, as the vector configuration is such that each  $\frac{\varphi_0}{2}$  rotation maps  $\vec{B}$  into its vertical image. That is to say, the angles formed by  $\vec{B}(\beta)$  and  $\vec{B}(\beta + \frac{\varphi_0}{2})$  with the tetrahedral axes define vertical, congruent pairs. Note that this is always true for  $B_\perp$ , but the symmetry is broken by the presence of a finite  $B_z$ . As  $B_z$  is taken to 0 the vertical symmetry becomes realized. A full  $4\pi$  rotation map is shown in Fig. 6. In this figure, the discrete rotational symmetry of the NV tetrahedron is clearly visible with the bright peaks within the middle of the plot.

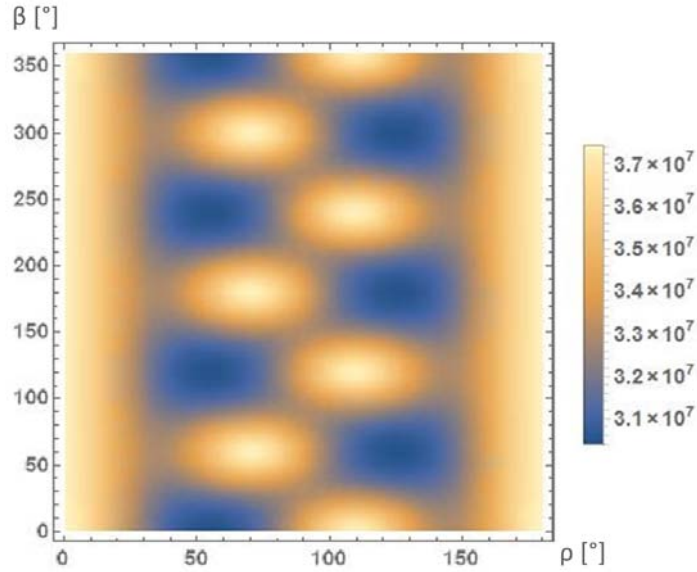


Figure 6: A full  $4\pi$  rotation map of the NV tetrahedron.  $\rho$  is the polar angle of the external magnetic field and  $\beta$  is the azimuthal angle.  $|B|$  is .01T and  $\Gamma$  is set to 10.

## 4 DETECTION OF MAGNETIC FIELDS

The aim of this work is to develop a method of detecting small magnetic fields. In many current methods of NV magnetometry an external bias field is established to provide a reference for the unknown perturbing fields. With this in mind, for the analysis that follows, the total magnetic field will be comprised of two terms: the known bias field and the unknown perturbing field, ie.  $\vec{B} = \vec{B}^0 + \vec{b}$ . The goal is to calculate  $\vec{b}$  in terms of  $\vec{B}^0$  (a known parameter) and observations on  $\vec{B}$ . To do this, the problem will be broken up into 2 parts: developing a method to determine  $b_{\parallel}$  and developing a method to determine  $\vec{b}_{\perp}$ . With this information the entire vector  $\vec{b}$  can be reconstructed.

### 4.1 Parallel Fields

It is predicted that near the Level Avoided Crossing (LAC) regions the PL intensity will be highly responsive to small, transverse field perturbations, as can be seen in Fig. 7. The LAC regions are found when  $B_z = \hbar D_{gs}/\mu g$ ,  $\hbar D_{es}/\mu g$ , or  $B_z \approx .103T, .051T$  respectively. It is interesting to note that with finite  $B_{\perp}$ , 3 regions appear which are symmetric under small variations in  $B_z$  - the 2 LAC regions and the midpoint between them<sup>9</sup>.

It can be imagined that a biasing external field is established such that the NV center is placed within one of these 3 symmetric regions. Then, being regions of high sensitivity, the magnitude of the parallel projection of the perturbing field can be determined from the difference in the observed sig-

<sup>9</sup> Note that  $B_z = 0$  is not considered in this analysis although it is a location where  $\frac{\partial S}{\partial B_z}$  vanishes and, when including the negative projections, indeed forms a symmetry point. The reason for its omission is that the curvature is poor at that location and thus from a practical consideration it is eliminated as a possibility.

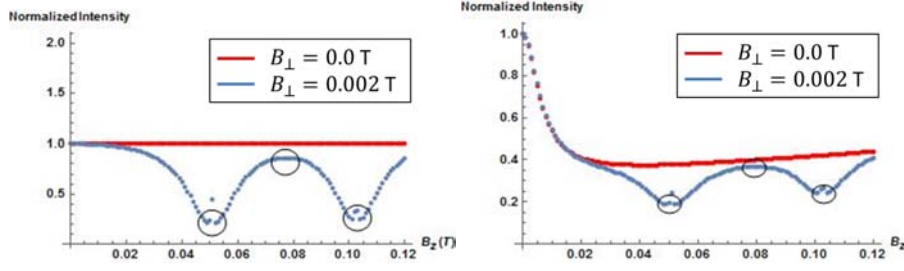


Figure 7: A demonstration of the increased sensitivity of the NV center to perturbing transverse fields around the LAC regions  $\sim .05\text{T}$  and  $\sim .1\text{T}$ . On the left is the single NV case, while on the right the full ensemble is considered. Circled are the 3 symmetry points about which a perturbing parallel field could be readily identified with the methods discussed in the text.  $\Gamma = 10$  in both cases. The small deviations that occur near the LAC points are due to divergences in the coefficients  $\alpha_{ij}$  that develop as a manifestation of the Perturbation Theory and are not physical.

nal and the signal predicted at the symmetry point. Only the magnitude of the parallel perturbation can be immediately determined from the observed signal due to the symmetry of the region; however, the sign of the perturbation can be obtained by shifting the biasing field off the symmetry point by a small amount and observing the change in the signal.

Mathematically, this is to say that at the symmetry point  $\frac{\partial S}{\partial B_z} = 0$  but elsewhere  $\frac{\partial S}{\partial B_z} \neq 0$  and thus has a sign. Therefore by measuring the sign of  $\frac{\partial S}{\partial B_z}$ , along with the direct measurement of  $S$  the parallel perturbation can be determined uniquely. This method of determining the parallel projection of the perturbing field will be referred to as the symmetric approach.

A claim might be made to use the regions of maximum slope rather than minimum slope as the biasing points as these regions will exhibit the largest sensitivity to parallel variations. However, the curvature profile of the signal is a function of the transverse perturbing field and so the specific location of maximum slope is not known a priori. The location of the local minima is, as it will always occur at the LAC point. Therefore it is recommended to use one of these extrema points as the bias points as they will be symmetric with any value of  $B_x$ .

For small perturbations, an expansion can be performed around the symmetry points:

$$S(B_z) \approx S(p_i) + \left. \frac{\partial^2 S}{\partial B_z^2} \right|_{p_i} \frac{(B_z - p_i)^2}{2} + \left. \frac{\partial^4 S}{\partial B_z^4} \right|_{p_i} \frac{(B_z - p_i)^4}{24} + \dots \quad (26)$$

where  $p_i$  denotes a symmetry point:  $\sim .05\text{T}$ ,  $\sim .075\text{T}$ , or  $\sim .1\text{T}$ . Here only even derivatives are nonzero due to symmetry considerations. For sufficiently small perturbations  $B_z - p_i$  the higher order terms can be neglected and the perturbation can be solved for directly:

$$S(B_z) = S(p_i) + \left. \frac{\partial^2 S}{\partial B_z^2} \right|_{p_i} \frac{(B_z - p_i)^2}{2}$$

$$\frac{\partial S}{\partial B_z} = \left. \frac{\partial^2 S}{\partial B_z^2} \right|_{p_i} (B_z - p_i)$$

Therefore:

$$\begin{aligned} b_z &= \frac{\partial S}{\partial B_z} \left( \frac{\partial^2 S}{\partial^2 B_z} \Big|_{p_i} \right)^{-1} \\ &\approx \frac{\Delta S}{\Delta B_z} \left( \frac{\partial^2 S}{\partial^2 B_z} \Big|_{p_i} \right)^{-1} \end{aligned} \quad (27)$$

where  $b_z \equiv B_z - p_i$ . Generally  $\frac{\partial^2 S}{\partial^2 B_z} \Big|_{p_i}$  is a function of  $B_\perp$  and the optical pumping parameter  $\Gamma$  and can be extracted by curve-fitting a signal profile such as that shown in Fig. 7. Unfortunately,  $B_x$  is not a fully known quantity, as it will contain a perturbation as well. It is yet to be seen if there is an optimal  $\Gamma$  value which minimizes the dependence of  $\frac{\partial^2 S}{\partial^2 B_z} \Big|_{p_i}$  on  $B_x$ , in which case the dependence of the signal curvature on  $B_x$  can be neglected to good approximation and the symmetric approach can be applied in all experimental situations. An alternative approach would be to determine  $B_x$  before attempting to quantify  $b_z$ ; a method of measuring  $B_x$  will be discussed later in the section.

In Eq. 27  $\frac{\Delta S}{\Delta B_z}$  is a measurable quantity; however by direct inspection of Fig. 7 it is clear that  $\frac{\partial S}{\partial B_z}$  is degenerate, but the locations of equal  $\frac{\partial S}{\partial B_z}$  are locations of unequal  $S$  for  $|b_z| < |p_i|$ . Therefore it is recommended to observe the signal as well as the response of the signal to small changes in  $B_z^0$  to determine the perturbation  $b_z$ .

It is important to recall the presence of the other NV modes as a strong magnetic field parallel to one axis will be strongly transverse to the other axes. This effect can be seen in Fig. 7 for the ensemble case, where even in the absence of a finite  $B_x$  there is a sharp drop in PL intensity. This is a manifestation of the effect seen in Fig. 3 in which an increasing transverse field drops the PL intensity. However, even in the ensemble case the LAC regions still demonstrate considerable sensitivity to transverse perturbations. Furthermore, in this model the number of total NV centers used is a simple multiplicative factor in the signal calculation, so with enough NV centers the signal can always be made sufficiently high to be detectable. As such, even in the case of ensembles the symmetric approach will be applicable.

A potential problem arises, however, by biasing the NV ensemble around the symmetric regions, as the transverse fields experienced by the other NV modes are of comparable strength to the zero-field splitting of the spin states. This model was derived with perturbative methods assuming transverse fields will be small, and so selecting such strong transverse fields may interfere with the perturbative approximation. Therefore only the excited state LAC region will be used in the remainder of this thesis with the understanding that more accurate results can be obtained by more elegant approximation methods, such as expanding around the LAC regions, for example.

## 4.2 Transverse Fields

### 4.2.1 $\beta$ Rotations

In considering transverse perturbations it is useful to properly define the geometry being considered. Fig. 8 demonstrates the most general type of perturbing field. In the figure,  $\Psi$  is the angle between the perturbing field

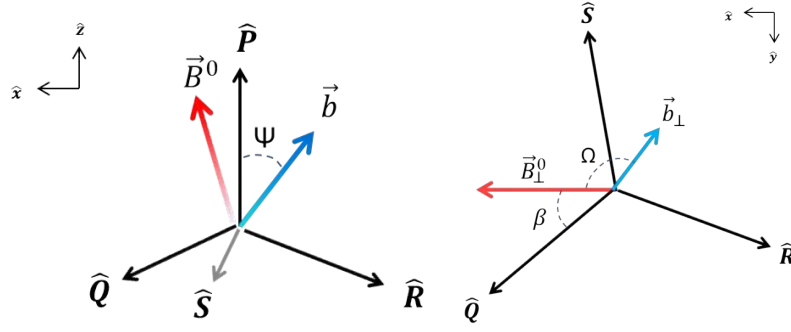


Figure 8: The geometry of the perturbing magnetic field.  $\Psi$  is the angle between the perturbing field and the z-axis, and  $\Omega$  is the angle between the perturbing field and the x-axis.

and the z-axis, and  $\Omega$  is the angle between the perturbing field and the x-axis. To simplify the analysis, in the presence of a perturbing field the x-axis will be redefined to lie along the transverse projection of the total magnetic field. This rotation can be alternatively viewed as a change of  $\beta$ , the angle between the tetrahedral axes and the x-axis.

An ambiguity exists when determining the cause of an observed  $\beta$ -shift as both the magnitude of the perturbing field and will orientation will determine the  $\beta$ -shift. Indeed, from simple geometry:

$$\tan(\delta\beta) = \frac{b_{\perp} \sin \Omega}{B_{\perp}^0 + b_{\perp} \cos \Omega} \quad (28)$$

Or after rearrangement:

$$b_{\perp} = \frac{B_{\perp}^0 \sin(\delta\beta)}{\sin(\Omega - \delta\beta)} \quad (29)$$

Therefore, with knowledge of  $\Omega$  and the change in  $\beta$   $b_{\perp}$  can be extracted, or vice versa. Note the case where  $B_{\perp}^0 = 0$ . In this situation  $\Omega$  can be determined (mod  $\frac{2\pi}{3}$ ) by observing any transverse behavior. However in this case, since  $\Omega$  will be equal to  $\delta\beta$ ,  $b_{\perp}$  will be undetermined.

Unfortunately, observing the periodic signal profile that characterizes these  $\beta$  rotations may prove to be difficult to realize experimentally if the system is to be biased in the quasi-transverse regime. As can be seen in Fig. 5 the magnitude of the oscillatory  $\beta$  profile is very small, and without development of a formal noise model it is unknown if these signal changes will be observable. Clearly, to proceed further in the analysis it is required to develop a method of determining either  $b_{\perp}$  or  $\Omega$  that provides more experimentally-feasible observations

#### 4.2.2 Signal Curvature Profile

As can be seen in Fig. 9, changes in the transverse field will cease to directly influence the observed signal beginning at relatively small magnitudes; the only influence the unknown transverse field will have on the observed signal will be in determining the curvature of the signal profile. Therefore a possible method of extracting the transverse field magnitude would be to measure the curvature of the signal profile, and then the parallel field magnitude can be determined as well as the transverse orientation  $\Omega$ .

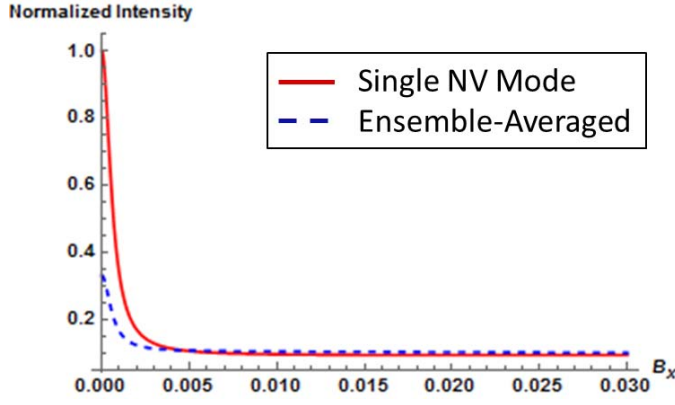


Figure 9: A plot demonstrating the effect of the transverse field on the observed signal when the system is biased around the excited state LAC. Clearly the observed signal approaches a steady value for  $B_x \gtrsim .002\text{T}$ . In generating this plot  $B_z = .05\text{T}$  and  $\Gamma = 10$ .

In general, the curvature of the signal profile will be a function of  $B_x$ ,  $B_z$ ,  $\beta$  and  $\Gamma$ . Near the symmetry points the curvature of the signal profile is approximately constant with respect to  $B_z$  (ie.  $\left. \frac{\partial^3 S}{\partial B_z^2} \right|_{p_i} = 0$ , as is dictated by symmetry). Therefore the signal curvature will not be influenced by the presence of a parallel perturbation. From Fig. 10 it is clear that the dominant source for changes in the observed signal curvature will be the presence of a transverse perturbation. Furthermore, the orientation of that perturbation has little influence on the change of curvature, only the magnitude of the perturbation will cause an observable change.

Fig. 11 plots the curvature of the excited state LAC as a function of  $B_x$ . To extract the  $B_x$  dependence a curve was fit to this plot, shown in green in the figure.  $\Gamma$  was set to 10 and  $\beta$  to 0. The functional form determined from this curve fitting procedure is:

$$\left. \frac{\partial^2 S}{\partial B_z^2} \right|_{p_i} \approx \frac{586038}{(B_x - .0005\text{T})^2} \quad (30)$$

Since  $B_x^2 = (\vec{B}_\perp^0 + \vec{b}_\perp)^2$ ,  $b_\perp$  can be solved for as:

$$b_\perp = -B_\perp^0 \cos \Omega \pm \sqrt{(B_{\perp, \text{Obs}}^2 - (B_\perp^0)^2) + (B_\perp^0)^2 \cos^2 \Omega} \quad (31)$$

where  $B_{\perp, \text{Obs}} \equiv \sqrt{586038 \left( \left. \frac{\partial^2 S}{\partial B_z^2} \right|_{\text{Obs}} \right)^{-1/2} + .0005\text{T}}$ .

Clearly when the observed perpendicular field matches the bias perpendicular field, the transverse perturbation is 0; however there is a negative solution ( $b_\perp = -2B_\perp^0 \cos \Omega$ ) predicted to exist as well. This solution is indicative of an underlying symmetry that is physical and may very well become manifest if the bias transverse field is nonzero. This symmetry, which shall be referred to as the “ $\beta$  symmetry” can be intuitively understood in Fig. 12, in which it is depicted as the “negative” solution for  $b_\perp$  given a positive angle  $\Omega$  or the “positive” solution for the negative angle (the latter will be the interpretation used in this analysis)<sup>10</sup>. An alternate method of understanding this symmetry is by considering the negative  $B_z$  branch of

<sup>10</sup> Positive angle refers to an angle belonging to the angular region  $[-\frac{\pi}{2}, \frac{\pi}{2}]$  in which  $\cos \Omega > 0$

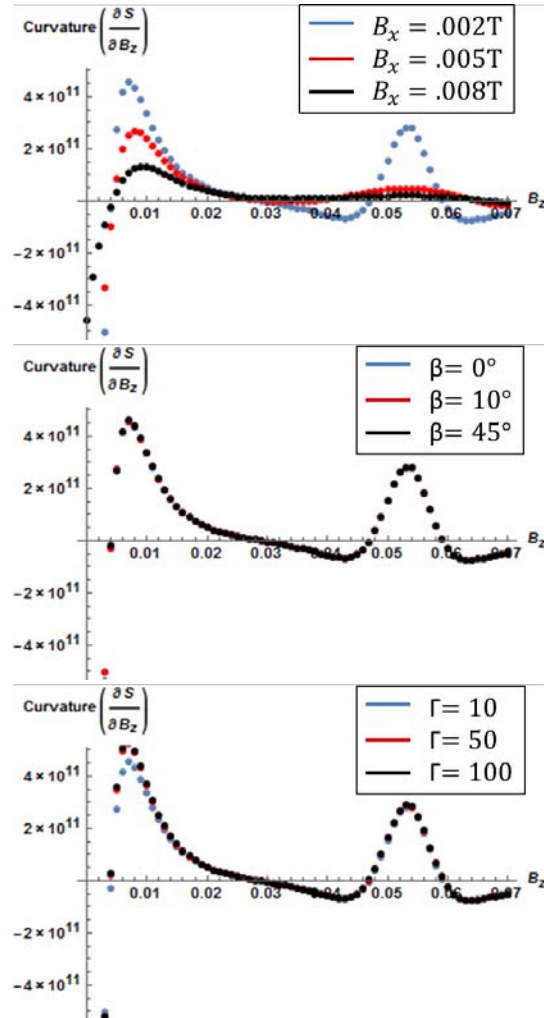


Figure 10: A series of plots depicting the dependencies of the signal curvature on  $B_x$  (Top),  $\beta$  (Middle) and  $\Gamma$  (Bottom). Clearly, a change in the transverse field magnitude is the dominant cause for changes in the observed signal curvature. It is therefore proposed that by monitoring the changes in the signal curvature the transverse perturbation magnitude can be determined.

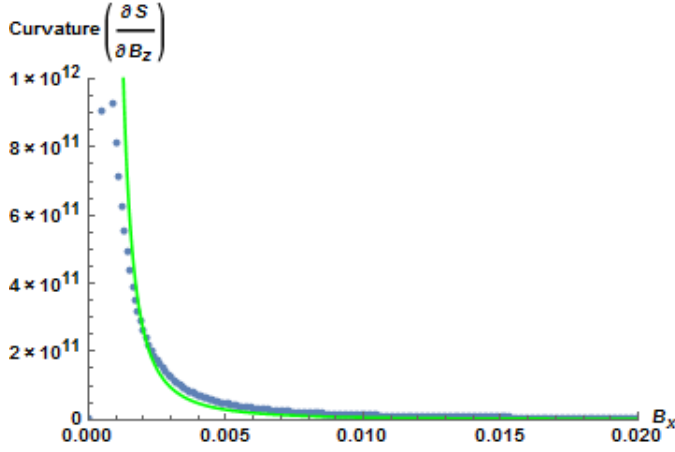


Figure 11: (Blue) A plot of the curvature of the signal profile evaluated at  $B_z = .052\text{T}$  and  $\Gamma = 10$  as a function of  $B_x$ . (Green) A fitted curve  $\left. \frac{\partial^2 S}{\partial B_z^2} \right|_{.052} = \frac{586038}{(B_x - .0005\text{T})^2}$  to extract the leading order dependence of the signal curvature upon  $B_x$ .

the curvature plot in Fig. 11. As the curvature has no dependence on  $\beta$ , in an unperturbed situation the transverse field can always be taken to be positive; however it could happen that a perturbation is perfectly anti-aligned with the bias transverse field and has a magnitude of  $2B_{\perp}^0$ . In this case  $B_{\perp}$  is effectively mapped to  $-B_{\perp}$ , which is an undetectable transformation with the sole observation of the signal curvature. Thus these “ $\beta$  symmetric” partners form a degenerate set, as there exists a continuum of allowed solutions due to the continuity of  $\cos \Omega$ .

When it is not the case that the observed transverse signal is equal to the bias transverse field the solutions are split into 2 regions:  $B_{\perp}^0 \leq B_{\perp, \text{Obs}}$  and  $B_{\perp}^0 > B_{\perp, \text{Obs}}$ . These two regions can be made more obvious with the substitution  $B_{\perp, \text{Obs}} = aB_{\perp}^0$  for an arbitrary  $a$ . Then, Eq. 31 becomes:

$$b_{\perp} = -B_{\perp}^0 \cos \Omega \pm B_{\perp}^0 \sqrt{a^2 - \sin^2 \Omega} \quad (32)$$

In this equation it is obvious that  $b_{\perp}$  will be degenerate under the mapping  $a \rightarrow -a$ . This is a manifestation of the rotational invariance of the system, and there is no loss of information by restricting  $a$  to be positive, as this is analogous to fixing the coordinate axes along the total transverse field. Furthermore,  $b_{\perp}$  will be double-valued with respect to the mapping  $\Omega \rightarrow -\Omega$  as the RHS of Eq. 32 is an even function of  $\Omega$ .

#### 4.2.3 $|a| \geq 1$ Solutions

The region  $B_{\perp}^0 \leq B_{\perp, \text{Obs}}$  corresponds to  $a \geq 1$ . In this case the term under the radical will always be positive. To obtain the correct limiting behavior as  $a \rightarrow 1$  the  $\pm$  in Eq. 32 must be handled properly. In doing this, the angular direction of  $b_{\perp}$  is limited to the quartercircle  $[0, \frac{\pi}{2}]$  and  $b_{\perp}$  is confined to be strictly positive:

$$b_{\perp} = -B_{\perp}^0 \left( \cos \Omega - \sqrt{a^2 - \sin^2 \Omega} \right) \quad \forall \Omega : 0 \leq \Omega \leq \frac{\pi}{2} \quad (33)$$

Note that no information is lost by limiting the angular distribution of  $b_{\perp}$  to this subregion as the full degeneracy of the solution is recovered by

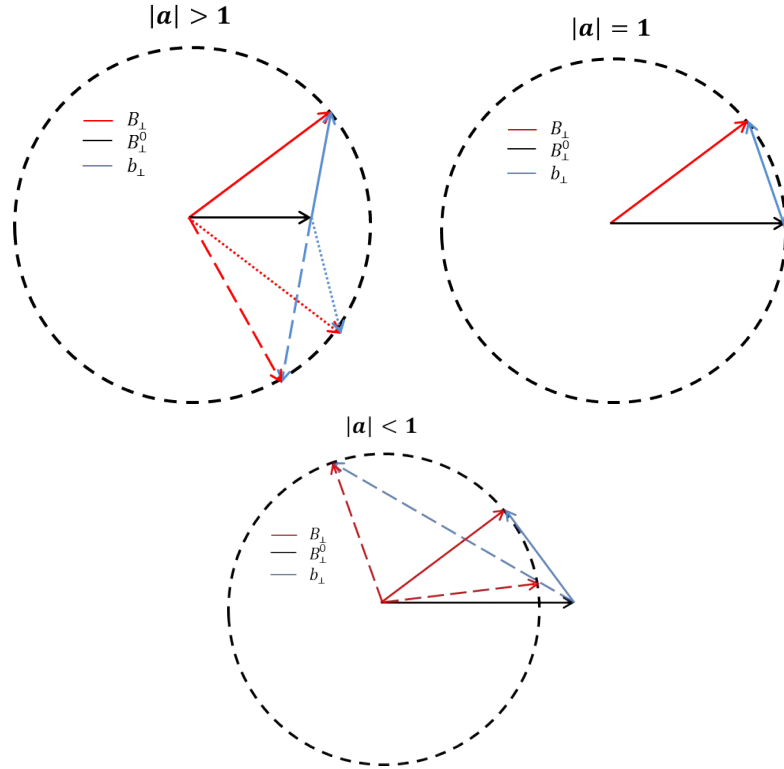


**Figure 12:** The rotational symmetry of the total transverse field (red). The dotted circle represents the projections of equal  $B_{\perp}$  and is what would be observed experimentally. For a fixed transverse bias field  $B_{\perp}^0$  (black), any transverse perturbing field  $b_{\perp}$  (blue) that creates a  $B_{\perp}$  with the observed magnitude is an allowable solution due to the rotational invariance of the signal curvature. For the case  $|a| \geq 1$  there is one positive solution for  $b_{\perp}$  for all values of  $\Omega$  in the range  $[0, 2\pi]$ . For the case  $|a| = 1$  there is one positive solution for  $b_{\perp}$  for all values of  $\Omega$  in the range  $[\frac{\pi}{2}, \frac{3\pi}{2}]$ . For the case  $|a| < 1$  there are only positive solutions for  $b_{\perp}$  for the negative angle interval when  $|\sin \Omega| \leq |a|$ . Usually there are 2 possible solutions on this interval, but when  $|\sin \Omega| = |a|$  there is only one tangent solution.

calculating the double-valued solutions with the mapping  $\Omega \rightarrow -\Omega$  for this region, and calculating the  $\beta$  symmetric partners. Given a transverse perturbation  $b_{\perp}^i$  at a given angle  $\Omega_i$  that solves Eq. 33, and a transverse bias field, the  $\beta$  symmetric partner can be calculated with the relationship:

$$\tilde{b}_{\perp}^i = b_{\perp}^i + 2B_{\perp}^0 \cos \Omega_i \quad (34)$$

The  $\beta$  symmetric set is then build up from the set of  $(b_{\perp}^i, \Omega_i)$  that constitute the positive solutions to Eq. 33.

It can be clearly seen that the  $\beta$  symmetric partners vanish if the transverse bias field is set to 0. This provides a simple means of removing the ambiguity in the observed curvature of the signal profile. Alternatively, the degeneracy can be partially lifted by probing the slope of the curvature profile in a similar manner as discussed for determining the magnitude of a parallel perturbation. If the slope is positive, then  $\vec{b}_{\perp} \cdot \vec{B}_{\perp}^0 < 0$ ; if the slope is negative, then  $\vec{b}_{\perp} \cdot \vec{B}_{\perp}^0 > 0$ .

#### 4.2.4 $|a| < 1$ Solutions

The region  $B_{\perp}^0 > B_{\perp, \text{Obs}}$  corresponds to  $a < 1$ . Now, the term under the radical in Eq. 32 may at times be negative, corresponding to the transverse perturbation having an imaginary component. This is not physical and thus places a bound on the allowed angular distribution of the transverse perturbation. Indeed, the bound becomes:

$$|\sin \Omega| \leq |a| \quad (35)$$

When  $|a| < 1$ ,  $\sqrt{a^2 - \sin^2 \Omega} < \cos \Omega$  for all choice of  $\Omega$ . This means that the two solutions for  $b_{\perp}$  will have the same sign, and thus will both be considered. This is unlike the previous case  $|a| \geq 1$  when the two solutions had opposite signs, and the negative solution was rejected in favor of the calculation of the  $\beta$  symmetric partner. For  $b_{\perp}$  to be strictly positive,  $\Omega$  must be further restricted to the negative angle regime  $[\frac{\pi}{2}, \frac{3\pi}{2}]$  in addition to the bound presented in Eq. 35. Since the RHS of Eq. 32 is even with respect to  $\Omega = \pi$ , without loss of information  $\Omega$  can be restricted to the negative quartercircle  $[\frac{\pi}{2}, \pi]$  with the understanding that degenerate solutions exist for the mapping  $\Omega \rightarrow -\Omega$ .

As seen in Eq. 32, for any  $\Omega$  such that  $|\sin \Omega| < |a|$  there are two allowable solutions for  $b_{\perp}$ . With the geometrical interpretation given in Fig. 12 these 2 solutions can be considered a secant solution. The tangent solution, or the solution when  $b_{\perp}$  is singularly valued for a given angle, occurs when  $|\sin \Omega| = |a|$ .

It is corroborative to the analysis that the solutions produced by the  $1/B_x^2$  dependence of the signal curvature produce degenerate solutions that encode  $\beta$  invariance of the curvature. This matches the graphical observations of Fig. 10.

If  $\Omega$  is unknown, then the following bounds can be placed on  $b_{\perp}$ :

$$|B_{\perp, \text{Obs}} - B_{\perp}^0| \leq b_{\perp} \leq B_{\perp, \text{Obs}} + B_{\perp}^0 \quad (36)$$

as can be clearly seen from Fig. 12. Notice that the difference between the maximum possible perturbation and the minimum possible perturbation is equal to  $2B_{\perp}^0$ ; as the magnitude of the transverse bias field is reduced the transverse perturbation can be more tightly bound. When  $B_{\perp}^0 = 0$  the magnitude of the transverse perturbation can be unambiguously identified.

#### 4.2.5 Experimental Procedure

The second derivative of the observed signal can be discretized in the following manner:

$$\left. \frac{\partial^2 S}{\partial B_z^2} \right|_{p_i} \approx \frac{S(p_i + \zeta) - 2S(p_i) + S(p_i - \zeta)}{\zeta^2} \quad (37)$$

where  $\zeta$  is a small offset to the biasing field.

Combined with Eq. 27 it is clear that the parallel and transverse projections of the perturbing field can be determined by performing 3 separate measurements: a first at  $B_z^0 \approx .05T$  to observe the overall signal, a second at  $B_z^0 \approx .05T + \zeta$  to extract the slope of the signal, and finally a third measurement at  $B_z^0 \approx .05T - \zeta$  to extract the curvature of the signal. With these three quantities the parallel projection can be calculated with Eq. 27. From the curvature measurement the parameter  $a$  can be extracted, and then the transverse perturbation can be restricted to reside in one of two regimes:  $|a| \geq 1$  and  $|a| < 1$ . The  $|a| \geq 1$  regime is defined by Eq. 33, Eq. 34, and the understanding that degenerate solutions exist for the mapping  $\Omega \rightarrow -\Omega$ ; the  $|a| < 1$  regime is defined by Eq. 32, Eq. 35, the additional restriction of  $\Omega$  to the negative quartercircle  $[\frac{\pi}{2}, \pi]$  and the understanding that degenerate solutions exist for the mapping  $\Omega \rightarrow -\Omega$  over this angular region.

As the technique for detecting parallel perturbations requires a finite transverse field, if this is to be true for all possible perturbations then the external bias field must have a finite transverse component. The presence of a finite transverse bias field means that observations of the transverse perturbation will suffer inherent ambiguities that will require the simultaneous measurement of the the third derivative of the signal profile ( $\frac{\partial C}{\partial B_x}$  for  $C \equiv \left. \frac{\partial^2 S}{\partial B_z^2} \right|_{p_i}$ ) and the  $\beta$  rotation of the perturbation to fully resolve. The first of these is possible by performing a second series of measurements at slightly offset transverse bias field (ie.  $\frac{\partial C}{\partial B_x} \approx \frac{1}{\epsilon} \left( \left. \frac{\partial^2 S}{\partial B_z^2} \right|_{p_i, B_x + \epsilon} - \left. \frac{\partial^2 S}{\partial B_z^2} \right|_{p_i, B_x} \right)$ ), necessitating 6 measurements in total. However, the observation of the  $\beta$  rotation will be difficult to observe in the quasi-parallel regime and may in turn require the bias field be shifted into the quasi-transverse regime for a larger oscillation amplitude.

Alternatively, the magnitude of the transverse field can be detected unambiguously by setting the bias field to have no transverse component, in which case any transverse effects, such as the formation of signal curvature or a  $\beta$  rotation, can be directly attributed to the presence of a transverse perturbation. With no transverse bias field, the ability to detect parallel perturbations with the symmetric approach is limited to cases when there simultaneously exists a finite transverse perturbation. However this inconvenience can be neglected by instead using the existing methods of parallel field detection which do not require the presence of a finite transverse field, such as the observation of ESR spectra or via Ramsey pulse sequencing. In this way transverse perturbations can be detected with relative simplicity.

Due to the  $\beta$  invariance of the signal curvature, no information regarding the angular orientation of the transverse perturbing field can be obtained in the absence of a transverse bias field. This can be remedied by performing a second measurement of the signal curvature with a small but nonzero transverse bias field. As the magnitude of the transverse perturbation will have been calculated from the signal curvature measurements with zero

transverse bias field,  $\Omega$  can then be determined up to the double-valued degeneracy of the mapping  $\Omega \rightarrow -\Omega$ .

## 5 CONCLUSION

There are many situations when it is desired to detect the presence of a small external magnetic field. The Nitrogen-Vacancy defect in diamond is capable of precise magnetometry in ambient conditions by observing changes in the fluorescence signatures. While many sophisticated methods of detecting fields parallel to the defect axis exist, these methods are unable to detect transverse fields. The all-optical method of NV magnetometry provides such a method of transverse field detection via the observation of an overall decrease in PL intensity associated to the spin state mixing induced by the transverse field. In this thesis the all-optical method of magnetometry is extended to consider ensembles of non-interacting NV centers.

It is found that the excited state LAC region exhibits high sensitivity to transverse fields. By biasing one of the defect axes of the NV ensemble around this region it is shown that through the measurement of the PL intensity drop, the slope of the signal curve and the curvature of the signal curve the magnitude of a parallel perturbation can be calculated. Furthermore, through the measurement of the signal curvature, a limiting bound can be placed on the magnitude of a transverse perturbation whose width is proportional to the transverse component of the biasing field. When the bias field is perfectly aligned with a defect axis and thus has no transverse component, the magnitude of the transverse perturbation can be unambiguously identified. It is therefore recommended that for the detection of transverse fields an external magnetic field perfectly aligned with a defect axis be applied to bias the system in the excited state LAC regime. If desired, the angular orientation of the transverse perturbation can be determined up to a two-fold degeneracy by repeating the measurement of the signal curvature with the bias field shifted slightly off-axis. For the detection of parallel fields an additional small biasing field transverse to the chosen defect axis must additionally be applied to the system to ensure that a finite curvature is always present in the signal profile.

### 5.1 Future Work to Be Explored

1. As can be seen clearly in Eq.16 and Fig.7 unfortunate divergences develop at the LAC regimes. While this does not impact the overall results it does make it difficult to characterize the immediate vicinity of the LAC regions with the present model. A more proper approach will assume the parallel field to be at the excited state LAC region and expand around variations about that point. Only the coefficients  $\alpha_{ij}$ ,  $i, j \in 4, 5, 6$  are expected to change with this new perturbation approach as the perturbation condition  $\frac{\mu g B}{\hbar D_{gs}} \ll 1$  is still maintained at the excited state LAC region.
2. A proper noise model should be developed with the photon shot noise as the dominant source of uncertainty. A demonstration of how this calculation might proceed is given in the appendix; however, the effort was ultimately unsuccessful due to the divergences that developed in

the attempts to place a bound on the minimum detectable field with the error expressions developed.

3. There exist two isotopes of nitrogen:  $N^{14}$  and  $N^{15}$ .  $N^{14}$  is the more prominent of the two and carries spin-1. Therefore its nuclear spin will interact with magnetic fields via Zeeman interactions and with the NV electronic spin via hyperfine interactions. The total Hamiltonian is composed of three parts: the NV electron Hamiltonian, the  $N^{14}$  Hamiltonian and the interaction Hamiltonian[44–46].

$$\begin{aligned} H_{\text{Tot}} &= H_{\text{NV}} + H_{N^{14}} + H_{\text{NVN}^{14}} \\ H_{N^{14}} &= \hbar Q I_z^2 + \hbar \gamma_N \vec{B} \cdot \vec{I} \\ H_{\text{NVN}^{14}} &= A_z S_z I_z + A_{\perp} (S_x I_x + S_y I_y) \end{aligned} \quad (38)$$

where  $Q = -4.95\text{MHz}$  is the intrinsic quadrupolar interaction of the nuclear spin,  $\gamma_N = -308\text{kHz/T}$  is the gyromagnetic ratio of the nuclear spin, and  $A_z = -2.162\text{MHz}$ ,  $A_{\perp} = -2.62\text{MHz}$  are the parallel and transverse components of the hyperfine tensor respectively.

In normal operations the effect of the local nuclear spin can be neglected but near the LAC regions these effects become more prominent[47]. The hyperfine interactions can create spin state mixing between states such as  $|m_s, m_I\rangle = |0, 0\rangle$  and  $|m_s, m_I\rangle = |+1, -1\rangle$  if these states are close in energy ie. at the LAC region, which in turn will influence the PL intensity. The accuracy of this model will be improved by included such effects.

## 6 APPENDIX

### 6.1 Approximate Nullspace of $M$

For the most general  $M$ , it is nontrivial to solve the Eq. 21 exactly. However, it is solvable numerically and with proper approximations it is solvable analytically as well. For the analytical approach, it is helpful to express the coefficients  $\alpha_{ij}$  explicitly in terms of small parameters that can then be used in expansions. The following new variables are defined:

$$\begin{aligned} \delta_a &= \frac{\mu g B_{\perp}}{D_{gs}} \\ \epsilon_a &= \frac{\mu g B_{\parallel}}{D_{gs}} \end{aligned} \quad (39)$$

$\delta_a$  and  $\epsilon_a$  are reduced, unitless representations of  $B_x$  and  $B_z$  respectively. In this representation, the four recurring non-trivial terms in the coefficients  $\alpha_{ij}$  are:

$$\begin{aligned}
\frac{\mu g B_{\perp}}{\sqrt{2}(\hbar D_{gs} - \mu g B_{\parallel})} &\rightarrow \frac{\delta_a}{\sqrt{2}(1 - \epsilon_a)} \\
\frac{\mu g B_{\perp}}{\sqrt{2}(\hbar D_{gs} + \mu g B_{\parallel})} &\rightarrow \frac{\delta_a}{\sqrt{2}(1 + \epsilon_a)} \\
\frac{\mu g B_{\perp}}{\sqrt{2}(\hbar D_{es} - \mu g B_{\parallel})} &\rightarrow \frac{\delta_a}{\sqrt{2}(D_{es}/D_{gs} - \epsilon_a)} \\
\frac{\mu g B_{\perp}}{\sqrt{2}(\hbar D_{es} + \mu g B_{\parallel})} &\rightarrow \frac{\delta_a}{\sqrt{2}(D_{es}/D_{gs} + \epsilon_a)}
\end{aligned} \tag{40}$$

Recall that the perturbative methods used to determine the coefficients  $\alpha_{ij}$  require  $\delta_a \ll 1$ . Therefore keeping only leading order in  $\delta_a$ , successive row reduction is performed until the matrix  $M$  is of the form

$$\begin{pmatrix}
* & * & * & * & * & * & * \\
& * & * & * & * & * & * \\
& & * & * & * & * & * \\
& & & * & * & * & * \\
& & & & * & * & * \\
& & & & & * & * \\
& & & & & & * & *
\end{pmatrix}$$

at which point direct inspection reveals the bottom row terms to be negligibly small and they are subsequently taken to be zero. Thus, by hand, the matrix  $M$  is forced to have a one-dimensional nullspace with the unnormalized nullvector  $\vec{n}$ .

## 6.2 Noise Model

Mathematically speaking, the results obtained from solving Eq. 24 yield the expected photon signal when averaged over the system's statistical distribution function. In order to develop a model to characterize the noise in the predicted signal, it is necessary to consider the sources of statistical uncertainty. The dominant source will be the photon shot noise, which follows Poisson statistics [48,49]. The shot noise appears through the rates  $k'_{ij}$ ; therefore it will be imposed that for a given collection time  $\tau$ :

$$\langle k'_{ij}{}^2 \rangle \tau^2 = \langle k'_{ij} \rangle^2 \tau^2 + \langle k'_{ij} \rangle \tau \tag{41}$$

as is dictated by Poisson statistics.

In quantum mechanics, the variance in the expected value of a quantum operator is given by the formula:

$$\Delta o^2 = \langle \hat{O}^2 \rangle - \langle \hat{O} \rangle^2 \tag{42}$$

In light of Eq. 42 the Signal operator  $S$  is defined as:

$$S = \eta \tau \sum_{i=4}^6 \sum_{j=1}^3 k'_{ij} |i\rangle \langle i| \tag{43}$$

$S$  is defined such that the expected value of  $S$  when operating on a generic wavefunction  $|\psi\rangle$  yields Eq. 10. That is to say:

$$\langle S \rangle = \eta\tau \sum_{i=4}^3 \sum_{j=1}^3 \langle k'_{ij} \rangle \bar{n}_i \quad (44)$$

Thus Eq. 42 will be used with regards to  $S$  to develop the statistical uncertainty in the observed photon signal.

It is necessary to express the uncertainty in  $S$  as a function only of the expectation values  $\langle k'_{ij} \rangle$ , as they can be obtained via Eq. 6. For the term  $\langle S \rangle^2$  this is already accomplished; however for the term  $\langle S^2 \rangle$  to be a function of  $\langle k'_{ij} \rangle$  the Poisson statistics must be imposed.

Indeed,

$$\begin{aligned} S^2 &= \eta^2 \tau^2 \left( \sum_{i=4}^6 \sum_{j=1}^3 k'_{ij} |i\rangle \langle i| \right) \left( \sum_{m=4}^6 \sum_{n=1}^3 k'_{mn} |m\rangle \langle m| \right) \\ &= \eta^2 \tau^2 \sum_{i,m=4}^6 \sum_{j,n=1}^3 k'_{ij} k'_{mn} |i\rangle \langle i|m\rangle \langle m| \\ &= \eta^2 \tau^2 \sum_{i=4}^6 \sum_{j,n=1}^3 k'_{ij} k'_{in} |i\rangle \langle i| \end{aligned} \quad (45)$$

Therefore, taking the expectation value of Eq. 45 and using Eq. 41:

$$\begin{aligned} \langle S^2 \rangle &= \eta^2 \sum_{i=4}^6 \sum_{j=1}^3 \bar{n}_i \left( \langle k'_{ij}{}^2 \rangle \tau^2 + \sum_{n \neq j} \langle k'_{ij} k'_{in} \rangle \tau^2 \right) \\ &= \eta^2 \sum_{i=4}^6 \sum_{j=1}^3 \bar{n}_i \langle k'_{ij} \rangle \tau \left( 1 + \langle k'_{ij} \rangle \tau + \sum_{n \neq j} \langle k'_{in} \rangle \tau \right) \\ &= \eta^2 \sum_{i=4}^6 \sum_{j,n=1}^3 \bar{n}_i \langle k'_{ij} \rangle \tau (1 + \langle k'_{in} \rangle \tau) \end{aligned} \quad (46)$$

where we've also made use of the fact that for independent quantities  $a$  and  $b$ ,  $\langle ab \rangle = \langle a \rangle \langle b \rangle$ .

Eq. 46 can be recast as the matrix equation:

$$\langle S^2 \rangle = \eta^2 \bar{n} E \text{Diag}(\vec{1} + \tau K' \vec{G}) \tau K' \vec{G} \quad (47)$$

Therefore with Eq. 24 & 47 the variance of the observed signal can be expressed with the following equation:

$$\Delta S^2 = \eta^2 \left[ \bar{n} E \text{Diag}(\vec{1} + \tau K' \vec{G}) \tau K' \vec{G} - (R\tau)^2 \right] \quad (48)$$

## REFERENCES

- [1] P. P. Borbat, A. J. Costa-Filho, K. A. Earle, J. K. Moscicki, and J. H. Freed, "Electron spin resonance in studies of membranes and proteins," *Science*, vol. 291, no. 5502, pp. 266–269, 2001.
- [2] M. Kainosho, T. Torizawa, Y. Iwashita, T. Terauchi, A. Mei Ono, and P. Guntert, "Optimal isotope labelling for nmr protein structure determinations," *Nature*, vol. 440, pp. 52–57, Mar. 2006.

- [3] A. Ajoy, U. Bissbort, D. Lukin, M. L. Walsworth, R. and P. Cappellaro, "Atomic-scale nuclear spin imaging using quantum-assisted sensors in diamond," *Phys. Rev. X*, vol. 5, p. 011001, Jan 2015.
- [4] L. H. Greene, H. Li, J. Zhong, G. Zhao, and K. Wilson, "Folding of an all-helical greek-key protein monitored by quenched-flow hydrogen-deuterium exchange and nmr spectroscopy," *European Biophysics Journal: EBJ*, vol. 41, no. 1, pp. 41 – 51, 2012.
- [5] D. S. Klinger, E. Chen, and R. A. Goldbeck, "Probing kinetic mechanisms of protein function and folding with time-resolved natural and magnetic chiroptical spectroscopies," *International Journal of Molecular Sciences*, vol. 13, no. 1, pp. 683 – 697, 2012.
- [6] M. Zaiss, P. Kunz, S. Goerke, A. Radbruch, and P. Bachert, "Mr imaging of protein folding in vitro employing nuclear-overhauser-mediated saturation transfer," *NMR In Biomedicine*, vol. 26, no. 12, pp. 1815 – 1822, 2013.
- [7] A. W. P. Fitzpatrick, G. T. Debelouchina, M. J. Bayro, D. K. Clare, M. A. Caporini, V. S. Bajaj, C. P. Jaroniec, L. Wang, V. Ladizhansky, S. A. Muller, C. E. MacPhee, C. A. Waudby, H. R. Mott, A. De Simone, T. P. J. Knowles, H. R. Saibil, M. Vendruscolo, E. V. Orlova, R. G. Griffin, and C. M. Dobson, "Atomic structure and hierarchical assembly of a cross-beta amyloid fibril," *Proc. Nat Acad. Sc.*, vol. 110, no. 14, pp. 5468–5473, 2013.
- [8] I. Wang, S.-Y. Chen, and S.-T. D. Hsu, "Unraveling the folding mechanism of the smallest knotted protein, mjo366," *The Journal of Physical Chemistry B*, vol. 119, no. 12, pp. 4359–4370, 2015. PMID: 25741995.
- [9] L. T. Hall, C. D. Hill, J. H. Cole, B. Städler, F. Caruso, P. Mulvaney, J. Wrachtrup, and L. C. L. Hollenberg, "Monitoring ion-channel function in real time through quantum decoherence," *Proc. Nat Acad. Sc.*, vol. 107, pp. 18777–18782, Nov. 2010.
- [10] L. P. McGuinness, Y. Yan, A. Stacey, D. A. Simpson, L. T. Hall, D. Maclaurin, S. Praver, P. Mulvaney, J. Wrachtrup, F. Caruso, R. E. Scholten, and L. C. L. Hollenberg, "Quantum measurement and orientation tracking of fluorescent nanodiamonds inside living cells," *Nat. Nanotech.*, vol. 6, no. 6, pp. 358–363, 2011.
- [11] D. Maclaurin, L. Hall, A. Martin, and L. Hollenberg, "Nanoscale magnetometry through quantum control of nitrogen-vacancy centres in rotationally diffusing nanodiamonds," *NEW JOURNAL OF PHYSICS*, vol. 15, 2013.
- [12] S. Kaufmann, D. A. Simpson, L. T. Hall, V. Perunicic, P. Senn, S. Steinert, L. P. McGuinness, B. C. Johnson, T. Ohshima, F. Caruso, J. Wrachtrup, R. E. Scholten, P. Mulvaney, and L. Hollenberg, "Detection of atomic spin labels in a lipid bilayer using a single-spin nanodiamond probe," *Proc. Nat Acad. Sc.*, vol. 110, no. 27, pp. 10894–10898, 2013.
- [13] D. Le Sage, K. Arai, D. R. Glenn, S. J. DeVience, L. Pham, L. M. and Rahn-Lee, M. D. Lukin, A. Yacoby, A. Komeili, and R. L. Walsworth, "Optical magnetic imaging of living cells," *Nature*, vol. 496, pp. 486–9, Apr. 2013.

- [14] L. Childress, R. Walsworth, and M. Lukin, "Atom-like crystal defects: From quantum computers to biological sensors," *Phys. Today*, vol. 67, pp. 38–43, Oct 2014.
- [15] K. Schlenga, R. McDermott, J. Clarke, R. E. de Souza, A. Wong-Foy, and A. Pines, "Low-field magnetic resonance imaging with a high- $t_c$  dc superconducting quantum interference device," *Appl. Phys. Lett.*, vol. 75, no. 23, pp. 3695–3697, 1999.
- [16] A. Burlakov, V. Gurtovoi, A. Il'in, A. Nikulov, and V. Tulin, "Superconducting quantum interference device without josephson junctions.," *JETP Letters*, vol. 99, no. 3, pp. 169 – 173, 2014.
- [17] K.-L. Chen, S.-H. Liao, Y.-H. Chen, H.-E. Horng, L.-M. Wang, and H.-C. Yang, "Low-noise serial high-  $t_c$   $yba_2cu_3o_y$  superconducting quantum interference devices based on bicrystal junctions.," *IEEE Transactions on Applied Superconductivity*, vol. 25, no. 1, pp. 1 – 7, 2015.
- [18] J. Kitching, S. Knappe, and E. Donley, "Atomic sensors: A review," *Sensors Journal, IEEE*, vol. 11, pp. 1749 –1758, sept. 2011.
- [19] L. Lenci, A. Auyuanet, S. Barreiro, P. Valente, A. Lezama, and H. Failache, "Vectorial atomic magnetometer based on coherent transients of laser absorption in rb vapor," *Phys. Rev. A*, vol. 89, p. 043836, Apr 2014.
- [20] S. J. Bending, "Local magnetic probes of superconductors," *Advances in Physics*, vol. 48, no. 4, pp. 449–535, 1999.
- [21] D. Rugar, R. Budakian, H. J. Mamin, and B. W. Chui, "Single spin detection by magnetic resonance force microscopy," *Nature*, vol. 430, no. 6997, pp. 329–332, 2004.
- [22] H. J. Mamin, M. Poggio, C. L. Degen, and D. Rugar, "Nuclear magnetic resonance imaging with 90-nm resolution," *Nat. Nanotech.*, vol. 2, pp. 301–306, 2007.
- [23] J. Miller, "Diamond defects enable nanoscale nuclear magnetic resonance.," *Physics Today*, vol. 66, no. 4, pp. 12 – 14, 2013.
- [24] L. Rondin, J.-P. Tetienne, T. Hingant, J.-F. Roch, P. Maletinsky, and V. Jacques, "Magnetometry with nitrogen-vacancy defects in diamond.," *Reports on Progress in Physics*, vol. 77, no. 5, p. 056503, 2014.
- [25] Y. Fu, H. Du, and J. Miao, "Patterning of diamond microstructures on si substrate by bulk and surface micromachining," *J. of Mat. Proc. Tech.*, vol. 132, pp. 73–81, Jan. 2003.
- [26] J. R. Rabeau, S. T. Huntington, A. D. Greentree, and S. Praver, "Diamond chemical-vaport deposition on optical fibers for fluorescence waveguiding," *Appl. Phys. Lett.*, vol. 86, p. 134104, 2005.
- [27] G. Balasubramanian, P. Neumann, D. Twitchen, M. Markham, R. Kolesov, N. Mizuochi, J. Isoya, J. Achard, J. Beck, J. Tissler, V. Jacques, P. R. Hemmer, F. Jelezko, and J. Wrachtrup, "Ultralong spin coherence time in isotopically engineered diamond," *Nat. Mater.*, vol. 8, no. 5, pp. 383–387, 2009.

- [28] K. Ohashi, T. Rosskopf, H. Watanabe, M. Loretz, Y. Tao, R. Hauert, S. Tomizawa, T. Ishikawa, J. Ishi-Hayase, S. Shikata, C. L. Degen, and K. M. Itoh, "Negatively charged nitrogen-vacancy centers in a 5 nm thin 12c diamond film," *Nano Letters*, vol. 13, no. 10, pp. 4733–4738, 2013.
- [29] M. E. Trusheim, L. Li, A. Laraoui, E. H. Chen, O. Gaathon, H. Bakhru, T. Schroder, C. A. Meriles, and D. Englund, "Scalable fabrication of high purity diamond nanocrystals with long-spin-coherence nitrogen vacancy centers," *Nano Letters*, vol. 1, no. 14, pp. 32–26, 2013.
- [30] J.-P. Tetienne, L. Rondin, P. Spinicelli, M. Chipaux, T. Debuisschert, J.-F. Roch, and V. Jacques, "Magnetic-field-dependent photodynamics of single nv defects in diamond: an application to qualitative all-optical magnetic imaging," *New Journal of Physics*, vol. 14, no. 10, p. 103033, 2012.
- [31] A. O. Sushkov, N. Chisholm, I. Lovchinsky, M. Kubo, P. K. Lo, S. D. Bennett, D. Hunger, A. Akimov, R. L. Walsworth, H. Park, and M. D. Lukin, "All-optical sensing of a single-molecule electron spin," *Nano Letters*, vol. 14, no. 11, pp. 6443–6448, 2014.
- [32] N. B. Manson, J. P. Harrison, and M. J. Sellars, "Nitrogen-vacancy center in diamond: Model of the electronic structure and associated dynamics," *Phys. Rev. B*, vol. 74, no. 10, pp. 104303–+, 2006.
- [33] M. W. Doherty, N. B. Manson, P. Delaney, F. Jelezko, J. Wrachtrup, and L. C. Hollenberg, "The nitrogen-vacancy colour centre in diamond," *Physics Reports*, vol. 528, no. 1, pp. 1 – 45, 2013. The nitrogen-vacancy colour centre in diamond.
- [34] J. Martin, N. Manson, D. Doetschman, M. Sellars, R. Neuhaus, and E. Wilson, "Spectral hole burning and raman heterodyne signals associated with an avoided crossing in the nv centre in diamond," *Journal of Luminescence*, vol. 86, p. 355, 2000.
- [35] J. Harrison, M. J. Sellars, and N. B. Manson, "Optical spin polarisation of the n-v centre in diamond," *Journal of Luminescence*, vol. 107, no. 1-4, pp. 245 – 248, 2004. Proceedings of the 8th International Meeting on Hole Burning, Single Molecule, and Related Spectroscopies: Science and Applications.
- [36] G. Balasubramanian, I. Y. Chan, R. Kolesov, M. Al-Hmoud, J. Tisler, C. Shin, C. Kim, A. Wojcik, P. R. Hemmer, A. Krueger, T. Hanke, A. Leitenstorfer, R. Bratschitsch, F. Jelezko, and J. Wrachtrup, "Nanoscale imaging magnetometry with diamond spins under ambient conditions," *Nature*, vol. 455, pp. 648–51, Oct. 2008.
- [37] V. R. Horowitz, B. J. Alemán, D. J. Christle, A. N. Cleland, and D. D. Awschalom, "Electron spin resonance of nitrogen-vacancy centers in opticallytrapped nanodiamonds.," *Proc. Nat Acad. Sc.*, vol. 109, pp. 13493–13497, Aug. 2012.
- [38] S. Hong, M. Grinolds, L. Pham, D. Le Sage, L. Luan, R. Walsworth, and A. Yacoby, "Nanoscale magnetometry with nv centers in diamond.," *MRS BULLETIN*, vol. 38, no. 2, pp. 155 – 161, 2013.

- [39] M. Grinolds, M. Warner, K. De Greve, Y. Dovzhenko, L. Thiel, R. Walsworth, S. Hong, P. Maletinsky, and A. Yacoby, "Subnanometre resolution in three-dimensional magnetic resonance imaging of individual dark spins," *Nat. Nanotech.*, vol. 9, pp. 279–284, Apr. 2014.
- [40] M. Loretz, T. Rosskopf, J. M. Boss, S. Pezzagna, J. Meijer, and C. L. Degen, "Single-proton spin detection by diamond magnetometry," *Science*, 2014.
- [41] L. Luan, M. S. Grinolds, S. Hong, P. Maletinsky, R. L. Walsworth, and A. Yacoby, "Decoherence imaging of spin ensembles using a scanning single-electron spin in diamond.," *Scientific Reports*, p. 8119, 2015.
- [42] P. Neumann, *Towards a room temperature solid state quantum processor - the nitrogen-vacancy center in diamond*. PhD thesis, Universitat Stuttgart, Holzgartenstr. 16, 70174 Stuttgart, 2012.
- [43] J. H. N. Loubser and J. A. van Wyk, "Electron spin resonance in the study of diamond," *Reports on Progress in Physics*, vol. 41, no. 8, pp. 1201–1248, 1978.
- [44] B. Smeltzer, J. McIntyre, and L. Childress, "Robust control of individual nuclear spins in diamond," *Phys. Rev. A*, vol. 80, p. 050302, Nov 2009.
- [45] A. Ajoy and P. Cappellaro, "Stable three-axis nuclear-spin gyroscope in diamond," *Phys. Rev. A*, vol. 86, p. 062104, Dec 2012.
- [46] M. Chen, M. Hirose, and P. Cappellaro, "Measurement of transverse hyperfine interaction by forbidden transitions," *arXiv:1503.08858*, 2015.
- [47] C. Wei and N. B. Manson, "Experimental investigations of the absorption and dispersion profiles of a strongly driven transition: Two-level system with a weak probe," *Phys. Rev. A*, vol. 49, no. 6, pp. 4751–4764, 1994.
- [48] C. A. Meriles, L. Jiang, G. Goldstein, J. S. Hodges, J. Maze, M. D. Lukin, and P. Cappellaro, "Imaging mesoscopic nuclear spin noise with a diamond magnetometer," *J. Chem. Phys.*, vol. 133, no. 12, p. 124105, 2010.
- [49] B. E. A. Saleh and M. C. Teich, *Fundamentals of photonics*. Wiley series in pure and applied optics, Hoboken, N.J. : Wiley-Interscience, c2007., 2007.

MIT OpenCourseWare  
<http://ocw.mit.edu>

## 22.THT Undergraduate Thesis Tutorial

Fall 2015

For information about citing these materials or our Terms of Use, visit: <http://ocw.mit.edu/terms>.